National Oceanography Centre
NATURAL ENVIRONMENT RESEARCH COUNCIL

EUMETSAT

EUMETSAT INVITATION TO TENDER 14/209556

JASON-CS SAR MODE SEA STATE BIAS STUDY

FINAL REPORT

CLARE BELLINGHAM, MERIC SROKOSZ, CHRISTINE GOMMENGINGER, PAOLO CIPOLLINI & HELEN SNAITH

NATIONAL OCEANOGRAPHY CENTRE – SOUTHAMPTON, UK

DECEMBER 2016

VERSION 1.0

DOCUMENT SIGNATURE TABLE

	Name	**Institution**	**Date**
Prepared by	Clare Bellingham, Meric Srokosz, Christine Gommenginger	NOC	12/12/2016
Authorized by	Christine Gommenginger	NOC	12/12/2016

ISSUE RECORD

Issue No.	Issue Date	Sections affected	Relevant information
V0.1	28/09/2016	All	First draft (incomplete)
V0.2	30/09/2016	Section 4.5.2	Added L2 1Hz SSH results
V1.0	12/12/2016	All	Complete version including revisions following first review

DISSEMINATION

To:	Means
Remko Scharroo (EUM)	remko.scharroo@eumetsat.int
Hans Bonekamp (EUM)	Hans.Bonekamp@eumetsat.int
Christelle Ponsard (EUM)	Christelle.Ponsard@eumetsat.int
Clare Bellingham (NOC)	crbilhm@noc.ac.uk
Meric Srokosz (NOC)	mas@noc.ac.uk
Christine Gommenginger (NOC)	cg1@noc.ac.uk
Helen Snaith (BODC)	h.snaith@bodc.ac.uk
Paolo Cipollini (NOC)	cipo@noc.ac.uk

TABLE OF CONTENTS

EXECUTIVE SUMMARY

This document represents the final report of a study funded by EUMETSAT about SAR mode Sea State Bias (SSB) for the Sentinel-6/Jason-CS mission. The study comprises a critical review of SSB estimation methods in conventional (low-resolution mode or LRM) altimetry, theoretical considerations about the effect of swell on SAR altimeter waveforms and empirical investigations with Cryosat-2 SAR mode data to detect swell effects in L1B and Level 2 Sea Surface Height (SSH). The report concludes by summarising the basis for the selection and derivation of the SAR altimeter sea state bias correction algorithm and the methods available to calibrate and validate SAR mode SSB corrections.

Theoretical considerations based on simple SAR waveform modelling indicate that multi-peaked waveforms could occur in the presence of swell, but that effects become clearly detectable only when swell height exceeds 4 meters, which is relatively rare. In the case of the Cryosat-2 data examined in this study, only 2% of samples satisfied this condition.

Experimental investigations of Cryosat-2 SAR mode data in different swell conditions produce no consolidated evidence of swell effects. Although anomalous 20Hz waveforms are occasionally observed, no statistically detectable effect of swell is obtained in the overall results for average L1B waveform shapes and L2 1Hz SSH biases and precisions. However, it is stressed that analyses in this study were limited geographically by the availability of Cryosat-2 SAR mode acquisitions over the ocean that could be collocated with Envisat ASAR swell data. It is strongly advised that analyses should be repeated with a broader geographical scope, including data from the central Pacific and the Southern Ocean where high sea state and swell conditions are more prevalent. It is suggested that this could be achieved using Sentinel-3 SRTM and Sentinel-1 L2 swell products, should such data be available.

Empirical SSB estimation methods offer the only viable way forward at present to estimate SAR mode SSB. Parametric, non-parametric and hybrid methods are all relevant, noting that hybrid methods may provide more robust estimates in those high sea state and swell conditions that are less densely populated and where effects will be more significant. The development of SAR mode SSB corrections should include additional dependence on sea state development, which would be consistent with the tendency in LRM towards three-parameters SSB models (e.g. Tran et al., 2010b; Pires et al., 2016).

The challenges of calibrating and validating SAR mode SSB corrections are the same - i.e. no better, no worse - than for conventional altimetry. For SAR mode altimetry however, P-LRM offer a unique way of calibrating and validating SAR mode SSB against conventional altimetry by providing coincident range measurements that have been shown to be unbiased against conventional LRM. In the case of Sentinel-6/Jason-CS, interleaved SAR mode will deliver true LRM data that make it possible to tie the Jason-CS SAR mode mission to the long-term altimetric data record without the issues linked to the loss of precision seen for SAR burst-mode P-LRM.

1. INTRODUCTION AND SCOPE OF THIS DOCUMENT

This document is the final report of the EUMETSAT Jason-CS SAR Mode Sea State Bias Study (Invitation to Tender 14/209556). The activities in this study comprised five elements:

a) a critical review of past and current methods used to estimate sea state bias in low-resolution mode altimetry

b) theoretical considerations of possible effects of swell on SAR altimetry.

c) an empirical investigation based on Cryosat-2 SAR mode data to detect possible effects of swell on SAR altimeter waveforms and Level 2 Sea Surface Height (SSH).

d) recommendations for the selection and derivation of the SAR altimeter sea state bias correction algorithm, based on the outcome of the above investigations.

e) overview of methods applicable to calibrate and validate SAR mode sea state bias estimates.

The report is structured according to these activities as follows:

- Section 2 provides a detailed literature review of LRM SSB estimation methods.
- Section 3 presents the outcome of the theoretical investigation of the impact of swell on SAR altimeter waveforms
- Section 4 presents the results of empirical investigations of swell effects in Cryosat-2 L1b SAR waveforms and L2 SSH.
- Section 5 makes recommendations for the selection and derivation of the SAR altimeter SSB correction algorithm.
- Section 6 summarises the means to calibrate and validate the SAR altimeter SSB correction for the Sentinel6/Jason-CS mission.

2. REVIEW OF LOW-RESOLUTION MODE SEA STATE BIAS

2.1. INTRODUCTION TO SEA STATE BIAS

A radar altimeter makes three basic measurements: the range to the sea surface, from which sea surface height (SSH) is derived; the backscattered power, often used to estimate wind speed or the mean square slope variance (mss); and the significant wave height. Satellite altimeter measurements provide unique information for global ocean circulation studies, giving surface geostrophic ocean currents estimates from SSH on a planetary scale, and additionally global significant wave height and wind speed observations (Fu & Cazenave, 2001). Following continuing technological improvements, errors in radar altimeter SSH estimates have steadily decreased and are now of the order of only 1-2 centimetres (Nerem et al., 2006; Cazenave & Llovel, 2010). The sea state bias (SSB), caused primarily by the non-Gaussian nature of waves on the ocean surface, is now the largest source of uncertainty in obtaining accurate estimates of SSH, leading to errors of the order of a few percent of the significant wave height (H_s) if uncorrected (Chelton et al., 2001; Tran et al., 2010a).

Essentially, the SSB results in an error in altimetric ranging, affecting the measurement of SSH, caused by the presence of waves on the ocean surface. For conventional pulse-limited altimetry, also known as Low-Resolution-Mode (LRM) altimetry, SSB is often considered to consist of three components:

- Electromagnetic bias (EM bias): linked to the backscatter in a nadir-viewing geometry being dominated by stronger reflections from the wave troughs than from the wave crests.
- Skewness bias: linked to real ocean waves having flatter troughs and peakier crests than sinusoidal waves, leading to a change is the statistical distribution of surface elevation from Gaussian to non-Gaussian (Srokosz, 1986). This results in the distribution of ocean elevation being skewed low, and the median sea surface height being located lower than the mean sea surface height we want to measure.
- Tracker bias: linked to instrument effects and the algorithmic choices made to retrieve the geophysical information from the waveforms by retracking.

While the two first components are physical effects that affect all satellite altimeters in the same way, the tracker bias is instrument and processing specific. The last component is included in sea state bias corrections estimated empirically for satellite altimeters, for example, from collinear or cross-over analyses. For this reason, empirical sea state bias corrections have to be evaluated separately for each altimeter mission or after any major change in instrument characteristics or processing. This makes it more problematic to understand and correct for SSB and explains why the correction of SSB in LRM altimeter measurements continues to be a challenging problem despite over 30 years of research on the topic (for early work see: Jackson, 1979; Lipa & Barrick, 1981; Barrick & Lipa, 1985; and Srokosz, 1986).

Based on theoretical considerations, SSB is generally expressed in the following form:

$$SSB = -\varepsilon H_s$$

with the minus sign indicating that SSB lowers the estimate of the SSH. The SSB coefficient ε might be taken to be dependent on a variety of parameters including: H_s, U_{10}, backscattered coefficient σ^0, some measure of wave slope, some measure of wave period, the wave spectrum, and so on. Typically, ε is taken to be a constant (most recent example is $\varepsilon = 0.035$ for the SARAL/ALtiKa mission; Verron et al., 2015) until sufficient data are available to better characterise its dependence on other parameters. Note that the backscattered coefficient σ^0 measured by the altimeter is used to estimate wind speed, through a problematic relationship that also depends on sea state (see, for example, Gommenginger et al., 2002; Gourrion et al., 2002; Gommenginger et al., 2003a). Various formulations of ε in terms of other parameters are discussed and evaluated below.

2.1.1. A NOTE ON RADAR ALTIMETER OPERATING MICROWAVE FREQUENCIES

To-date most radar altimeters have operated at K_u band (13.6 GHz) microwave frequencies, though the recently launched SARAL/ALtiKa mission (Verron et al., 2015) operates at K_a band (35 GHz). Since the launch of Topex in 1992, most radar altimeters have operated at dual frequency: K_u with C band (5.3 GHz; Topex / Jason series, Sentinel-3 SRAL series) or with S band (3.2 GHz; Envisat) as a secondary measurement frequency to make a correction for the effect of the ionosphere on the travel time of the radar pulse to and from the sea surface. One issue, not pursued here, is the effect of SSB at other radar frequency measurements than K_u band. Some work has been done on this problem (e.g. Walsh et al., 1991, Arnold et al., 1995) but the use of a secondary frequency for ionospheric correction means that it is difficult to untangle the SSB effects on the measurements at these frequencies (see Stewart & Devalla, 1994). In what follows, the focus is on SSB corrections for K_u band radar altimeters, which is where most research effort has been expended.

2.1.2. SAR MODE ALTIMETRY AND SEA STATE BIAS

SAR Mode altimetry over the ocean was demonstrated for the first time in orbit with the ESA Cryosat-2 mission. Scientific studies since 2010 have convincingly demonstrated the improved performance of SAR altimetry in terms of reduced altimetric noise, finer along-track spatial resolution and improved performance near land (see Gommenginger et al., 2013a and references therein).

The review of the state of knowledge for SAR ocean altimetry commissioned by EUMETSAT and reported in Gommenginger et al. (2013a) highlighted that no solution was available as yet for sea state bias in SAR mode, and that there remained uncertainties about the sensitivity of SAR mode altimetry to long ocean surface waves (swell) and their direction of travel.

Preliminary investigations have suggested a possible impact of swell and swell direction on SAR altimetry. Numerical simulations (Moreau et al., 2013) and analyses of Cryosat-2 SAR mode waveforms in swell conditions (Gommenginger et al., 2013b) indicate that SAR

altimeter waveforms might be distorted in the presence of swell (broader leading edge, even possible double peaks). Hence, to the usual three components of sea state bias, one can add an additional source of uncertainty in SSH determination linked to swell and its direction relative to the SAR altimeter's smaller and strongly asymmetric footprint (along-track-resolution of the order of 300m). This term could be called a "swell bias" in SAR altimetry.

Before proposing possible SSB correction strategies for SAR altimetry, we review the SSB correction approaches that have been used for standard LRM radar altimetry. This will allow the critical assessment of which strategies might be applicable to SAR mode altimetry.

2.2. LRM SEA STATE BIAS ESTIMATION METHODS

Here we critically review the various methods available to estimate SSB for conventional LRM altimeters, focussing on the levels of uncertainty and means of validation. This will serve as the background against which we can ascertain the applicability and relevance of similar methods to the SAR altimetry SSB problem.

SSB corrections methods considered in this review include the following:

- Parametric and non-parametric methods applied to collinear and crossover differences (e.g. Chelton, 1994; Gaspar et al., 1994; Labroue et al., 2004)
- Direct SSB estimation methods with 2 or 3 parameters (e.g. Vandemark et al., 2002; Tran et al., 2010b)
- Hybrid SSB method (Scharroo & Lillibridge, 2004)
- Tower-based and airborne observations (e.g. Melville et al., 2004; Millet et al., 2003a; 2003b)
- Theoretical models (e.g. Srokosz, 1986; Elfouhaily et al., 2000; 2001)
- Numerical simulator methods (e.g. Amarouche et al., 2000; Naenna & Johnson, 2010)

The first three categories will be subsumed under the general theme of empirical methods as they are all derived from the altimeter observations themselves, while the other three will be treated individually.

2.2.1. EMPIRICAL METHODS

Parameteric and non-parametric methods are the most commonly used approaches to estimate sea state bias for satellite altimeter missions, and have a long history in the correction of SSB, going back to studies such as Gaspar et al. (1994) and Gaspar & Florens (1998), respectively, and earlier. Empirical approaches rely on the *assumption* that local changes in mean sea level (for example, due to currents and eddies) are uncorrelated with any changes in H_s. Therefore they optimise the sea state bias coefficient to explain as much of the SSH variability as possible.

The basic principle is to minimise SSH differences against chosen (what are considered) relevant parameters, typically significant wave height, H_s, and wind speed at a height of 10m above the sea surface, U_{10}. SSH differences are obtained either from repeat passes on the same track (collinear; e.g. Chelton, 1994), crossovers (e.g. Gaspar et al., 1994) or by considering the SSH residuals from the Mean Sea Surface (e.g. Vandemark et al., 2002). This leads to an estimate of SSB in terms of altimeter-measured quantities such as H_s and U_{10}, so that $\varepsilon = \varepsilon(H_s, U_{10})$ or, similarly, H_s and backscatter coefficient σ^0, so that $\varepsilon = \varepsilon(H_s, \sigma^0)$ (e.g. Scharroo & Lillibridge, 2004).

The best-known parametric method is probably the so-called BM4 model due to Gaspar et al. (1994), which reads:

$$e = a_1 + a_2 H_s + a_3 U_{10} + a_4 U_{10}^2 \qquad \text{Eq. 1}$$

where the constants a_n are estimated from data, using the collinear, crossover, direct or hybrid methods mentioned above. There is no *a priori* reason why this should be considered the correct functional form and the original Gaspar et al. (1994) consider a variety of functional forms, but all based on H_s and U_{10}. *A posteriori,* BM4 has been found to work reasonably well for the altimeters flown to-date.

To avoid having to specify a functional form for ε, non-parametric methods have been developed (e.g Gaspar & Florens, 1998). These estimate ε from SSH differences as in the parametric case, but do so simply by calculating ε on a two dimensional grid of H_s and U_{10}, thus avoiding specifying a functional form. This results in a "look-up table" (LUT) for ε. Although the non-parametric methods avoid the problems associated with assuming a particular parametric form, they still suffer from the *a priori* assumption that ε can be characterised in term of H_s and U_{10}. Based on empirical evidence (e.g. Arnold et al., 1995; Melville et al., 2004; Millet et al., 2005) and theoretical considerations (e.g. Srokosz, 1986; Glazman et al., 1996; Gommenginger et al., 2003b; Elfouhaily et al., 2000, 2001), this has been shown to not be the case.

The Vandemark et al. (2002) direct method uses SSH residuals from the Mean Sea Surface and has the advantage of requiring less data to derive a SSB correction. This means in practice that a SSB correction can be derived from altimeter observations earlier in an altimeter mission. The disadvantage of the method is that it requires Mean Sea Surface estimates, which may not be sufficiently reliable away from the tracks of earlier altimeter missions. Tran et al. (2010a) exploited the fact that the Topex, Jason-1 and Jason-2 missions have all used the same ground tracks, to sample the same Mean Sea Surface and derive improved and consistent corrections for the altimeters flown on these satellites over a 17-year period.

The two most recent new approaches to deriving SSB corrections are those of Scharroo & Lillibridge (2004) and Tran et al. (2010b). Both approaches build on the direct method of the Vandemark et al. (2002). Scharroo & Lillibridge (2004) proposed a hybrid method and use H_s and σ^0 to characterise the SSB. They use the direct method to obtain a binned (in H_s and σ^0) estimate of SSB. Then a version of the BM4 model (see above, with U_{10} replaced by σ^0) is fitted

and residuals calculated and smoothed. The smoothed residuals are re-combined with the BM4 model to give the final SSB correction.

Most recently, Tran et al. (2010b) proposed a three-parameter SSB correction, making use of mean wave period, T_m, from the WaveWatch III (WW3) numerical wave model, so that $\varepsilon = \varepsilon(H_s, U_{10}, T_m)$. Through this, they try to capture more subtle ranging errors linked to the degree of sea state development (as reported also by Gommenginger et al., 2003a; Melville et al., 2004). The disadvantages of this approach are: 1) whether the H_s and U_{10} measured by the altimeter are consistent with T_m obtained from the wave model; and 2) how accurate are the estimates of T_m from the wave model. Wave models have well-known deficiencies (Stopa et al., 2015), particularly in their ability to estimate wave period, which might affect the SSB correction. In addition, since numerical wave model performance depends on the quality of the wind forcing and the sophistication of its internal physical parameterisations, the SSB correction derived with T_m from a wave model will be specific to a particular version of the wave model, and will not be universally applicable to other missions.

Finally, as noted by Scharroo & Lillibridge (2004), there are problems with using U_{10} to characterise SSB, since wind speed algorithms differ from altimeter to altimeter (cf. Gommenginger et al., 2002; Gourrion et al., 2002). This is why Scharroo & Lillibridge (2004) use σ^0 instead. However, there are problems also with using σ^0 as altimeter radar backscatter coefficients are not absolutely calibrated. In practice, σ^0 from successive altimeters flown in space have to be adjusted to match those of previous altimeter missions, for example by applying an empirically determined bias (e.g. Zieger et al., 2009, Table 2).

2.2.2. TOWER-BASED AND AIRBORNE OBSERVATIONS

Tower-based experiments have the advantage of offering a stable platform and a long time series of measurements. The advantages of airborne campaigns are the freedom to sample a greater range of conditions (including much deeper waters far from the coast), no problems with tower structure influencing the wave field or radar, and options to fly at a variety of different heights. The first tower-based experiments to determine SSB were carried out by Yaplee *et al.* (1971). They showed that the variation in backscatter strength at X-band (10 GHz) was strongly in phase with the sea surface elevation distribution (rather than being biased towards the front or back face of waves), and that the variation was well described by a simple linear fit with wave height. Aircraft campaigns led to different values at different microwave frequencies: 3-5% of H_s at 10 GHz (Choy *et al*, 1984) and 1.1% of H_s at 36 GHz (Walsh *et al*, 1984). Note that Hevizi et al. (1993) found that the SSB at K_u and C band was dependent on the height of the airborne measurements (decreasing with increasing altitude).

More recent tower-based observations (Millet et al., 2003a; 2003b; Melville et al., 2004; Millet, 2005) have suggested that the SSB is related to the root-mean-square wave slope, and possibly wave age. Numerical evaluations of various SSB theories by Gommenginger et al. (2003b) have lent support to such dependence. Note that since altimeter data have shown dependence on wave period (e.g. Gommenginger et al., 2003a; Mackay et al., 2008) and mean

square slope together with H_s then, in principle, some measure of wave slope could be derived from the altimeter data. Kumar et al. (2003) evaluated a wave slope based SSB correction, with the wave slope taken from the WAM wave model, and concluded that this is a promising approach, but to-date this has not been implemented routinely for radar altimeter measurements.

A limitation of both the airborne and tower-based experiments is that they can only sample a limited range of conditions, which may not be representative of the global measurements being made by spaceborne altimeters. Towers are usually located in shallow water, and both towers and aircraft flights are usually fairly near the coast (for obvious reasons).

One further issue to be noted, more so with the tower-based than the airborne measurements, is that the sea surface is in the near field of the tower-based radar antenna. In contrast, the sea surface is in the far field of the antenna of a spaceborne instrument. Thus, in the tower-based case, the curvature of the radar electromagnetic wave front may match that of the undulation of the sea surface due to waves, giving a focussing effect, whereas in the spaceborne case, the curvature of the electromagnetic wave front is much larger than that of any wave induced undulation. Therefore, caution is advised when trying to tower-based and airborne results directly to spaceborne systems.

2.2.3. THEORETICAL MODELS OF SSB

Theoretical models of SSB go back to the work of Jackson (1979), Barrick & Lipa (1985) and Srokosz (1986), who proposed similar models accounting for weakly nonlinear waves at the sea surface with non-Gaussian statistics. These models depend on the work of Longuet-Higgins (1963) for their statistical description of the nonlinear sea surface waves. Elfouhaily et al. (2000, 2001) extended these studies to account for further nonlinear effects. The two theoretical models of Srokosz (1986) and Elfouhaily et al. (2000) were evaluated by Gommenginger et al. (2003b) in comparative analyses that included empirical SSB estimates from satellites (Gaspar et al., 1994) and from tower-based experiments (Melville et al., 1991; Millet et al., 2003a; 2003b). This study revealed an unexpected dependence of SSB on rms slope of the long waves, which is a standard parameter used in wave studies to characterise the nonlinearity of waves.

The more complicated Elfouhaily et al. (2001) theoretical model was evaluated only once against airborne measurements by Vandemark et al (2005). They find that the model gives a reasonable representation of the measured SSB. They conclude that both long wave nonlinearities and long-short wave interactions need to be considered in any empirical correction scheme for SSB, though they do not suggest how this might be done in practice.

The most recent theoretical model is due to Millet et al. (2006). This combines long wave non-Gaussian statistics with hydrodynamic modulation of short waves and tests the results against the tower-based observations of Arnold et al. (1995) and Millet et al. (2005). They find a dependence on the long wave slope variance, as Gommenginger et al. (2003b) and Melville

et al. (2004) did previously. How their model might be applied to correct SSB effects in altimeter data is unclear.

Note that theoretical models do not typically account for frequency dependence of SSB, other than indirectly e.g. by a frequency cut-off imposed on the wave spectrum. In addition, all models to-date only account for weakly nonlinear wave effects and cannot represent strongly nonlinear effects such as wave breaking. Finally, theoretical models do not account for instrument and processing effects, which may in some cases be the dominant cause of SSB.

2.2.4. NUMERICAL ESTIMATIONS OF SSB

Numerical simulators have also been used to evaluate the SSB error (Amarouche et al., 2000; Naenna & Johnson, 2010). The simulator requires an ocean waves module capable of producing 3D ocean surfaces with realistic non-linear surface waves, and the capacity of producing convincing altimeter waveforms. The retracked SSH in both modes can then be compared with the known SSH of the original 3D surface. The main drawback of the method is that it is computationally expensive, since the non-linear sea surface must be described with a spatial resolution that complies with the roughness criteria appropriate to the microwave radar scattering theory used to produce the altimeter data.

Naenna & Johnson (2010) perfectly illustrate the difficulties of the simulation approach. They simulate in 2-D only (assuming long-crested waves) a patch of ocean 1.4km long with an altimeter flying at 200km and estimate the resulting electromagnetic bias. They use a Pierson-Moskowitz spectrum for the wave field together with a model of the nonlinear sea surface due to Creamer et al. (1989). The surface is resolved down to scales of ~1cm and they perform 60,000 Monte Carlo realisations for each frequency (Ku, C, S band) and for each wind speed conditions considered, and for different resolutions of the simulated sea surface. They note that extending this simulation to realistic altimeter altitudes, i.e. larger patches of the sea surface, and a full 2-D ocean wave field is computationally prohibitive. They find that their simulation results are consistent with the Brown model and that there is a weak radar frequency dependence of the electromagnetic bias. They also find that the resolution at which the sea surface is simulated strongly affects the magnitude of the bias (their Figures 6 and 7).

To conclude, in any numerical simulation, the ability to simulate realistic altimeter waveforms need to be carefully validated. This is particularly true in SAR mode altimetry, where the shape of the SAR waveforms is strongly determined by the simulator's ability to account for the spatio-temporal decorrelation of the surface and the coherent/incoherent integration that characterise SAR altimetry. LRM and SAR mode waveforms from the Cryosat Mission Simulator (CRYMPS) were evaluated in the ESA SAMOSA study (Gommenginger et al., 2011) for various (linear) sea surface scenarios, showing some encouraging but ultimately unsatisfying results.

2.3. CRITICAL ASSESSMENT OF THE APPLICABILITY OF LRM SSB METHODS TO SAR ALTIMETRY

Numerical simulations can provide some insight into the mechanisms that determine SSB and the dependence of SSB on a variety of parameters, but cannot represent a practical solution to estimating SSB for two reasons. Firstly, today's simulations of ocean surfaces can at best only represent weakly nonlinear waves over the size of ocean patches needed to simulate spaceborne scenarios. Secondly, the computational cost of simulating the correct behaviour of the surface at the small scales sensed by the radar is prohibitive. For example, at K_u band, the radar wavelength (~2cm) will interact with waves on the sea surface at scales where surface tension effects become important, and for which the behaviour and modelling of the wave spectrum is not well understood (e.g. Figure 1 of Hwang & Plant, 2010).

Tower-based and airborne observations could be useful for providing insight into the SSB problem and to validate SSB corrections applied to spaceborne measurements but, as noted earlier, such measurements have not been routinely used to develop SSB corrections in LRM radar altimeter measurements of SSH. Similarly, theoretical models of the SSB have helped to shed important new light on the dependence of SSB on ocean parameters. Thus, the dependence of LRM SSB on rms slope of the long waves was confirmed using theoretical analyses, supported by evidence from tower-based experiments. In the case of SAR altimetry, there exist analytical models to model SAR waveforms theoretically (e.g. Ray et al., 2014), which could provide guidance on the way to deal with effects such as swell. However, it should be noted that these SAR altimeter models are significantly more complex and unwieldy than in the case of LRM, so that such investigations represent a non-trivial undertaking.

Finally, empirical methods offer the most practical and most commonly used approaches to determine an SSB correction, since they can be tailored to a particular instrument and therefore also account for instrument and processing effects. The main problem with all the empirical methods is to determine on which parameters to base the estimation of the SSB coefficient (i.e. H_s, U_{10}, σ^0, T_m, etc…) and where to source the data for these parameters (i.e. from the altimeter data, from models,..). In the case of SAR altimetry, if some measure of wave period and wave direction is needed to correct for swell bias, it is not clear at present where such information could be coming from, other than from numerical wave models.

2.4. CONCLUSIONS ON SEA STATE BIAS IN LOW-RESOLUTION MODE

The conclusion of Chelton et al. (2001) still stands with regard to SSB: "Improvements of the sea-state bias correction thus pose difficult challenges, both theoretically and observationally." This remains true for LRM altimetry, and even more so for SAR altimetry, given the possible influence of swell and swell direction due to the short and strongly asymmetric footprint of SAR altimeters.

The empirical methods developed for LRM are equally applicable to SAR mode altimetry and this must be the way forward in the first instance, for correcting for SSB in SAR-enabled

missions. The so-called “Interleaved mode” on the Jason-CS/Sentinel-6 mission provides the means of performing direct validation of the SAR mode SSB against the LRM SSB corrections that have been developed over the past few decades. This will not provide an absolute validation of either methods but at least provide the means to tying the Jason-CS/Sentinel-6 SAR mode data to the long-term altimetric time series.

3. THEORETICAL CONSIDERATIONS OF SWELL EFFECTS IN SAR ALTIMETRY

3.1. A VERY SIMPLE ARGUMENT

As scattering will be occurring from the crests and troughs of the swell, from above and below the mean sea surface respectively, the signature of that scattering will be seen in the SAR altimeter waveform as two peaks on either side of the leading edge (nominal position of the mean sea surface). The displacement of these peaks on either side of the leading edge will depend on the amplitude of the swell. For a SAR altimeter with a waveform bin width of ~3 nanoseconds, the height resolution will be ~ 45cm (two way travel time ct/2). This means that to detect double peaks in the waveforms they would need to be separated by at least one bin. Therefore, 3 bins are required to see separate radar reflections from the crests and troughs of swell waves, which means that such double peaks will NOT be detectable for waves with crests and troughs separated by less the 3 x 45 cm = 1.35m. In practice, with noise and sea as well as swell waves, this would suggest that you need reasonably high swell waves. For simple narrowband spectrum swell H_{swell} = √2 x (crest-to-trough height) = 1.414 x ~1.35m = ~1.9m. This implies that swell effects on the waveform will only be detectable in the waveforms for conditions when swell H_{swell} > 1.9m or thereabouts.

3.2. A SIMPLE GEOMETRICAL CONSIDERATION

Figure 1 (below) shows schematically the SAR altimeter footprint and swell travelling in various directions relative to the satellite travel direction. From the figure, given the highly elongated nature of the SAR altimeter footprint across-track, it is clear that swell waves travelling parallel or nearly parallel to the satellite travel direction will have a small number of crests (and troughs) within the footprint, whereas those travelling perpendicular or at other angles to the satellite track will have many crests (and troughs) within the footprint. This is a simple consequence of the fact that the swell wavelength $\lambda = O(d)$ and $d \ll L$, in terms of the dimensions of the footprint, so $L/\lambda \gg 1$ and $d/\lambda = O(1)$.

To determine (approximately) at what angle θ the situation changes from the near parallel case (few crest / troughs), to the more general case (many crests / troughs) is a straightforward calculation. From Figure 1(b) it is easily seen that the number of crests is given by $M \sim L / [\lambda/\sin(\theta))] = L \sin(\theta) / \lambda$. For the perpendicular case $N = L / \lambda$. Therefore if $M \ll N$ then $\sin(\theta) \ll 1$. For small θ, $\sin(\theta) \sim \theta$, so this leads to $\theta \ll 1$. If $\theta \sim 0.1 \ll 1$, say, then "near parallel" will mean swell travelling at angles less than (approximately) ±6° either side of the satellite track.

The consequence of this is that a statistical approach can be taken to the scattering in the general case (many crests / troughs; Figure 1a and Figure 1b), but a different approach is required for the parallel (or near parallel) travel case (Figure 1c). The two differing approaches are pursued below.

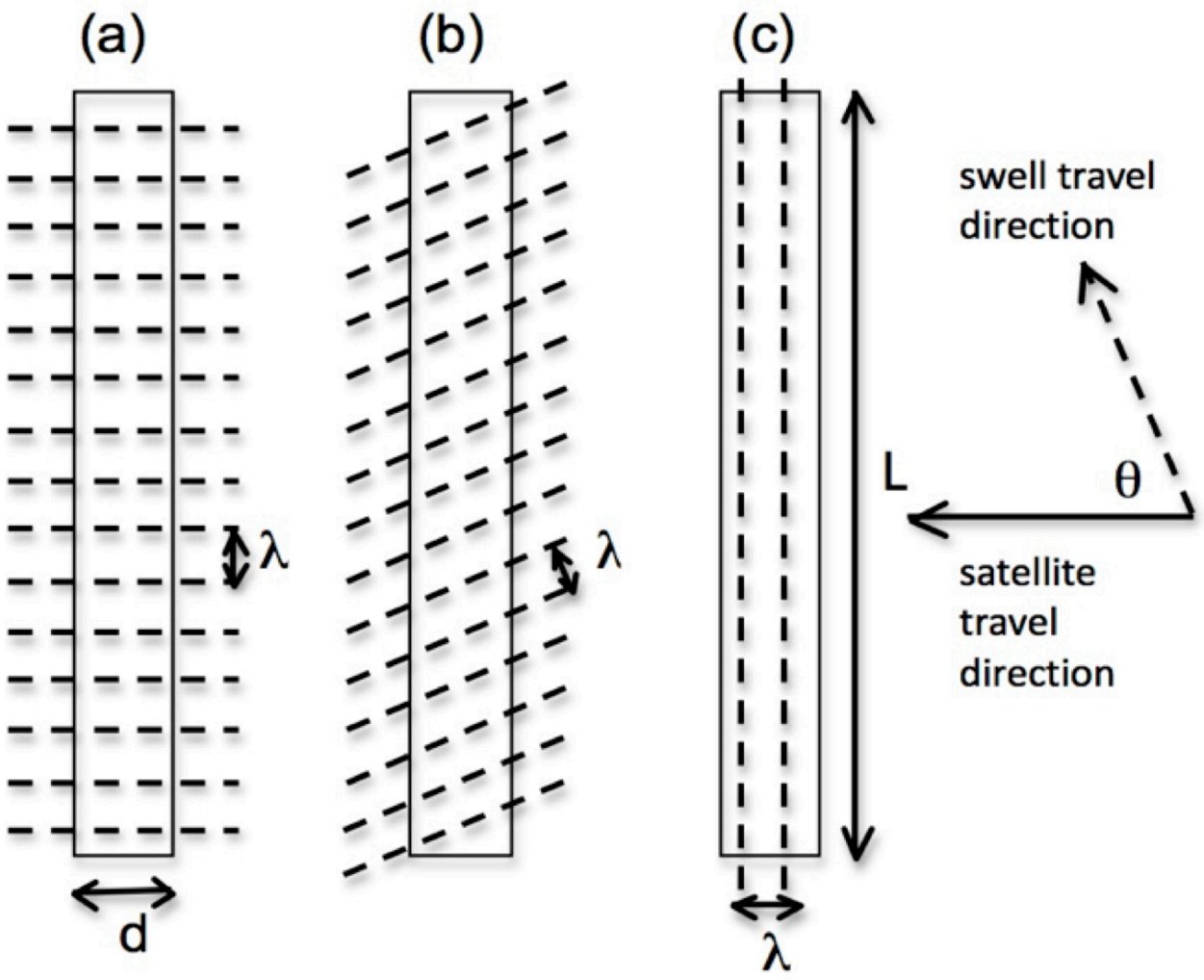

Figure 1: SAR altimeter footprint depicted as rectangular box with sides L x d, with L >> d (typically L ~ 7km and d ~ 300m). Swell crests (or troughs) depicted by dashed lines, with wavelength λ. Note that λ = O(d) i.e. typically 100-400m. Swell travel direction relative to satellite travel direction is measured by the angle θ. (a) swell perpendicular to satellite travel direction (θ = π/2 or 3π/2); (b) swell travel direction at some general angle θ; (c) swell parallel to satellite travel direction (θ = 0 or π).

3.3. A SIMPLE ANALYTICAL MODEL OF SAR ALTIMETER WAVEFORMS FOR "SEA PLUS SWELL" WAVES FOR THE GENERAL CASE OF SWELL CRESTS NOT PARALLEL TO THE SAR ALTIMETER FOOTPRINT

This model is based on the so-called SAMOSA3 model developed under an ESA contract (Ray & Martin-Puig, 2012). It has the advantage of being analytic, so is useful for exploring the possible effects of swell on the SAR altimeter return waveform in the open ocean. The key point to note is that it assumes that the scattering can be described by a pdf of specular points (scattering from the wave crests and troughs described statistically), which means that it is

NOT applicable to swell waves travelling parallel (or nearly parallel) to the satellite travel direction as only a small number of swell wave crests will fall in the SAR altimeter footprint, so a statistical description will fail to capture the radar scattering behaviour correctly (see discussion above and Figure 1). This case (parallel travel) will be discussed separately below.

The basic form of the SAMOSA3 SAR altimeter waveform is given by (after correction of typographical errors in Ray & Martin-Puig, 2012)[1]:

$$p(x) = P_0 \{1/\sqrt{s}\} \exp[-(x/s)^2/4] K_{-1/4}[(x/s)^2/4] / (2\sqrt{2}) \quad \text{for } x < 0 \qquad \text{Eq. 2}$$

and

$$p(x) = P_0 \{1/\sqrt{s}\} (\pi/\sqrt{x}) \exp[-(x/s)^2/4] \{I_{-1/4}[(x/s)^2/4] + I_{1/4}[(x/s)^2/4]\} \quad \text{for } x \geq 0 \qquad \text{Eq. 3}$$

where I and K are Bessel functions, P_0 depends on various parameters of the SAR altimeter and s is given by:

$$s(H_s) = \sqrt{[1/(2\ \alpha_g) + H_s^2/(4\ L_z^2)]} \qquad \text{Eq. 4}$$

where α_g and L_z are parameters of the SAR altimeter and H_s is the significant wave height of waves at the sea surface. Note that in this formulation mean sea surface is at x = 0 and x > 0 corresponds to returns from above the mean, while x < 0 to returns from below the mean. In addition, x is a scaled distance such that $x = (z / L_z)$, where z is in metres.

For illustrative purposes, in what follows $P_0 = 1$ (this assumption will be discussed later), $\alpha_g = 1.6831$ and $L_z = 0.4863$m, which are the Cryosat-2 values of the parameters (Ray & Martin-Puig, 2012). In this SAR altimeter waveform model, the mean sea surface is at x = 0, and returns from crests above the mean appear in the waveform for x < 0, while returns from troughs below the mean appear in the waveform for x > 0. Figure 2 illustrates the waveforms obtained for H_s = 1, 2, 4 and 8 m in the absence of swell waves.

3.3.1. MODELLING THE WAVEFORM RETURNS FROM SWELL WAVES

For simplicity, assume that that for the swell waves all the crests have the same height h_c above the mean sea level, and that all the troughs have the same depth h_t below mean sea level. Therefore, we can say that the return from the swell will be given by:

$$p_{swell}(x) = p(x+h_c) = p(x-h_t) \qquad \text{Eq. 5}$$

with s=s(0), i.e. H_s=0 (this simply implies no variability in h_c and h_t). Recall that returns from crests will precede (x < 0) those from troughs (x > 0). The swell waveheight in this very simple model is given by $H_{swell} = (h_c+h_t)$. If there were no sea (locally generated wind waves) this would lead to a double peaked return as illustrated in

[1] *Note that the analytic simplifications in terms of Bessel functions are based on the earlier work of Gommenginger at al. (2011).*

Figure 3 (below) for $h_c = h_t$ = 1, 2 and 4m (i.e. H_{swell} = 2, 4 and 8m). The separation of the peaks is simply a function of H_{swell}.

Note that for H_{swell} = 1m (not shown) the double peaks merge and cannot be distinguished, which is consistent with the very simple argument at the beginning of this section about the detectability of swell effects in the SAR altimeter returns.

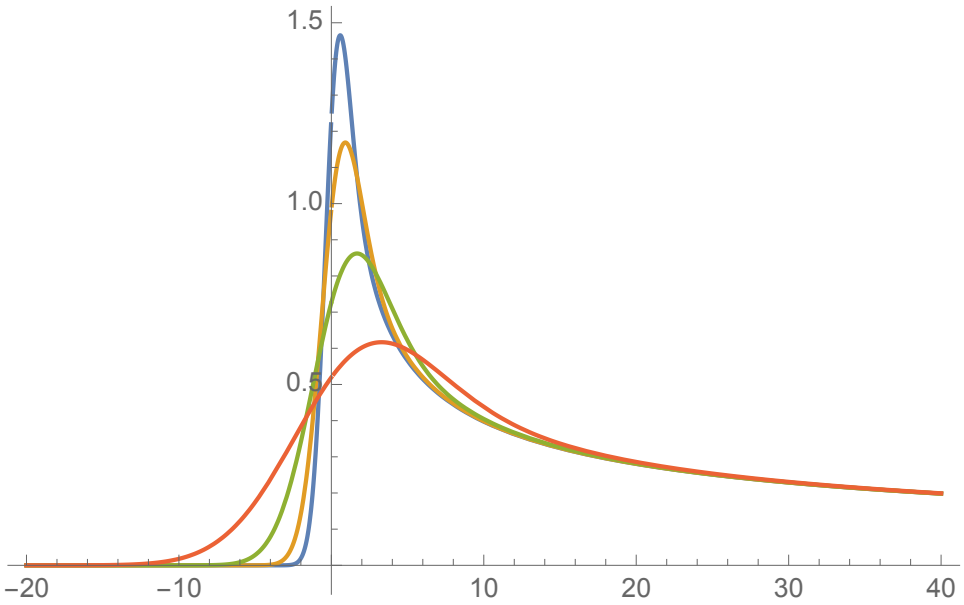

Figure 2: SAR altimeter waveform for significant wave height H_s = 1 (blue), 2 (tan), 4 (green) and 8m (orange).

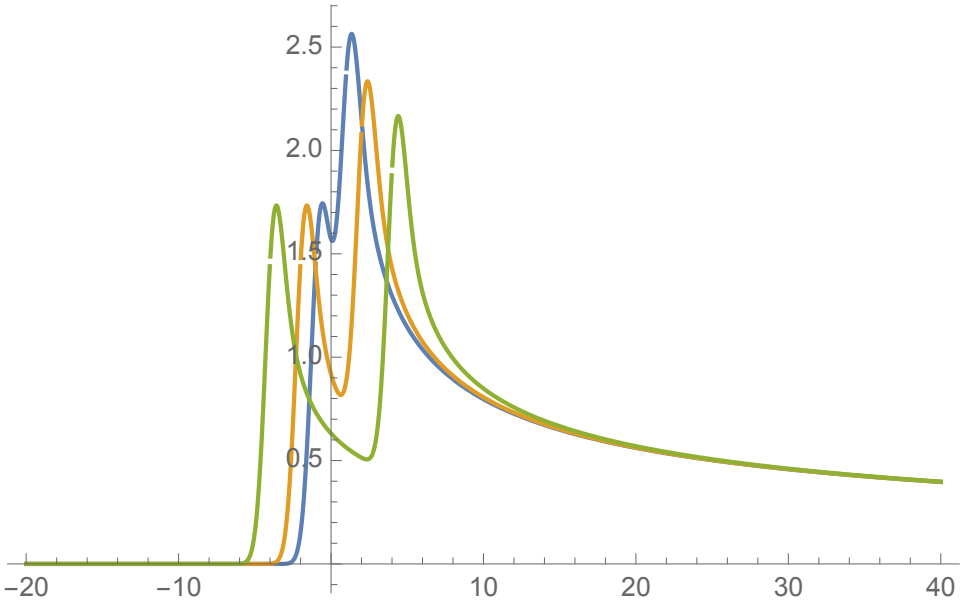

Figure 3: SAR altimeter waveform for swell waves with equal crest and trough heights $h_c = h_t$ = 1 (blue), 2 (tan) and 4m (green) corresponding to swell wave height of H_{swell} = 2, 4 and 8m. Modelling the waveform returns from "sea and swell".

Simply adding the swell-type waveforms to the sea-type waveforms produces the results displayed in Figure 4 to Figure 7 for significant wave height H_s = 1, 2, 4 and 8m respectively, with H_{swell} = 2, 4 and 8m in each plot.

Note the following behaviours:

- for H_{swell} = 2m, the presence of swell only distort the leading edge of the waveform slightly and the return only becomes double peaked at higher values of H_s = 4 and 8m. See blue curves in Figure 4 to Figure 7.
- for H_{swell} = 8m, a triple peaked structure is evident in the waveform for H_s = 1, 2 and 4m but the return becomes double peaked for H_s = 8m. See green curves in Figure 4 to Figure 7.
- for H_{swell} = 4m, behaviour intermediate to the two described above is found. See tan curves in Figure 4 to Figure 7.

From this it can be concluded that the presence of swell will distort the measured SAR altimeter waveform and so affect any estimates of geophysical parameters obtained by fitting a standard SAR altimeter model to the measurements. This could result in effects such a bias in the altimeter height measurement. It should be noted that H_{swell} of 8m is uncommon in the open ocean so the results for 2 and 4m are probably more realistic (blue and tan curves in Figure 4 to Figure 7).

Note that these analytic results are consistent with the limited numerical simulations of Moreau et al. (2013)[2] who found that large values of H_{swell} were required to distort the waveform leading edge, and even larger values to give the waveform a double peaked structure (their simulations use unrealistically large values of H_{swell} = 8 and 12m). As a consequence of using numerical simulation Moreau et al. (2013) are able to allow for changes in wavelength of the swell (not possible here due to the statistical nature of the analytical model) and their results suggest changes in swell wavelength have a significant effect on the waveform. In particular, shorter steeper swell waves have a larger effect. Note that they simulate swell with heights of 12m and 16m for a wavelength of 100m, which is physically unrealistic (theoretically the steepest wave has a height to wavelength ratio of ~0.142). However, the dominant effect seems to be due to the height of the swell, as seen here (in Figures 4 to 7). Interestingly Moreau et al. (2013) found the same double peaked structure in their simulations of the SAR altimeter waveform for both parallel (swell aligned with the SAR altimeter ground track) and non-parallel (swell perpendicular to the SAR altimeter ground track) geometry. They did not seem to consider swell directions intermediate between the

[2] *Note that the numerical simulations are intrinsically limited to a small number of cases because they are computationally intensive. A further issue is the resolution of the sea surface used in the simulations.*

parallel and perpendicular cases, but the analytic results here suggest that this double (or triple) peaked structure in the waveform will be present in those situations too.

It would seem from this analysis, given that real SAR altimeter waveforms will be distorted by noise, the detection of swell effects on measured waveforms might be problematic.

3.3.2. LIMITATIONS OF THIS ANALYSIS

There are a number of limitations to this analysis:

- Clearly the model could be used to investigate the effect of different crest heights and troughs relative to the mean surface, rather than the symmetrical situation considered here (with crest height above the mean equal to trough depth below the mean). In the open ocean swell waves do not usually display much nonlinearity, so the assumption made here is probably valid most of the time. Of course, on entering shallow water – typically defined as water depth less than ¼ of the swell wavelength – the nonlinearity of the waves will increase as they shoal and the crest heights and trough depths will become more asymmetric with respect to the mean surface (peakier crests, flatter troughs). However, in shallow waters close to land, altimeter data will be affected by a number of other issues including waveform shape distortion due to reflections from land and increased errors in tidal and wet tropospheric corrections, for which entirely different modelling and estimation approaches are needed.
- This analysis assumes that the scattering from the crests and the troughs of the swell and from the sea is identical (captured in the assumption that $P_0 = 1$ in equations 1 and 2 above). P_0 includes the backscattered power σ^0, which could (and almost certainly does) vary. This could be allowed for in the model changing P_0 for the swell crests and troughs and the sea returns. Unfortunately, it is not *a priori* obvious how to specify what values of P_0 should be used (for example, σ^0 varies with wind speed). However, allowing for this would simply change the relative strengths of the return from the swell crests and troughs and the sea, but would not fundamentally alter the observation that these combinations could lead to single, double or triple-peaked waveforms; possibly with a distorted leading edge in the single peak case.
- To understand the effects of the swell distortion of the SAR altimeter waveform on the retrieval of geophysical parameters would require fitting a standard model of the return to swell-affected waveforms, plus the inclusion of noise, over a range of geophysical conditions.

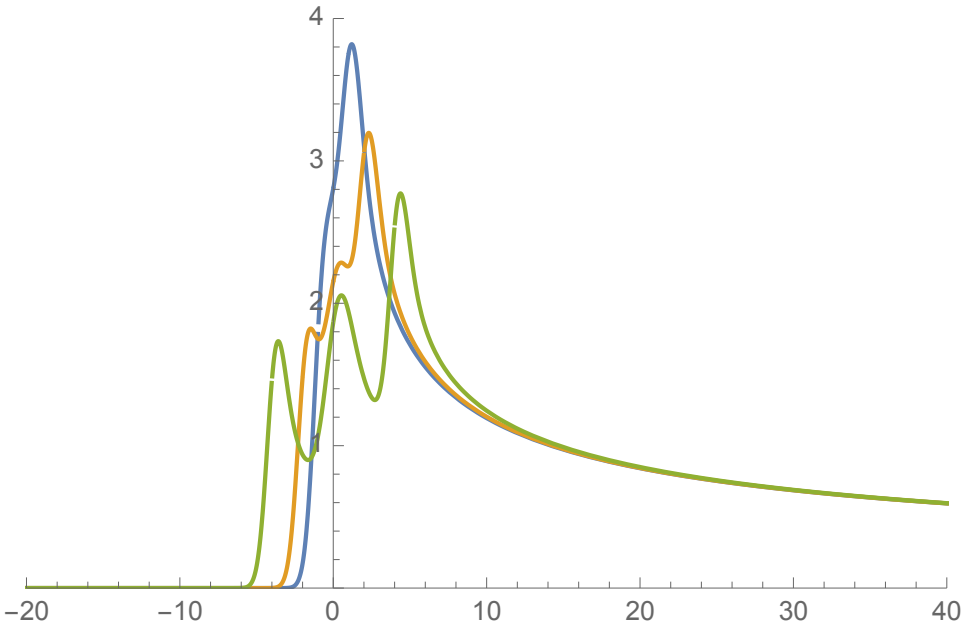

Figure 4: SAR altimeter waveform for significant wave height H_s = 1m and swell height H_{swell} = 2 (blue), 4 (tan) and 8m (green).

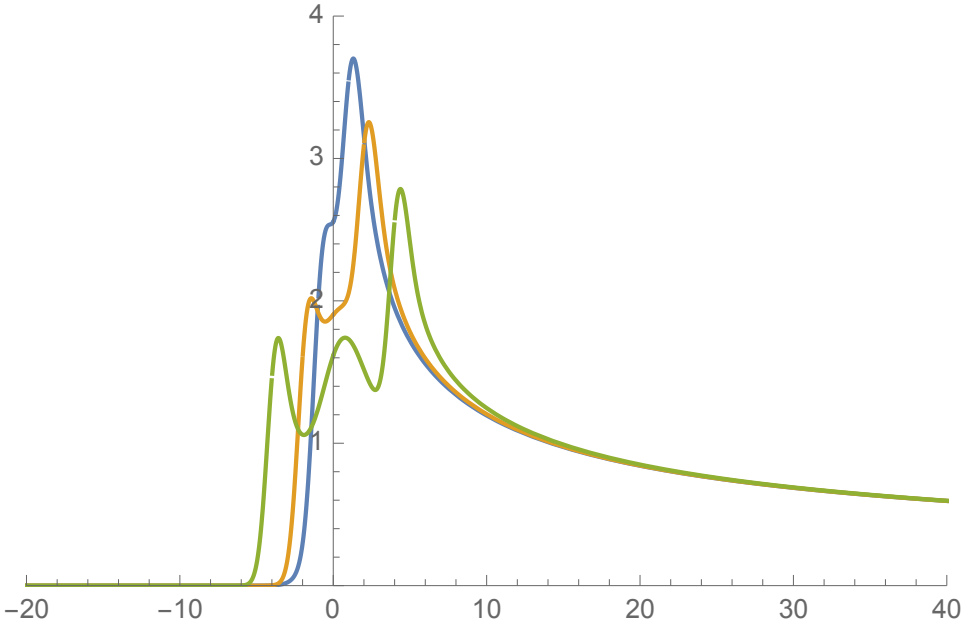

Figure 5: SAR altimeter waveform for significant wave height H_s = 2m and swell height H_{swell} = 2 (blue), 4 (tan) and 8m (green).

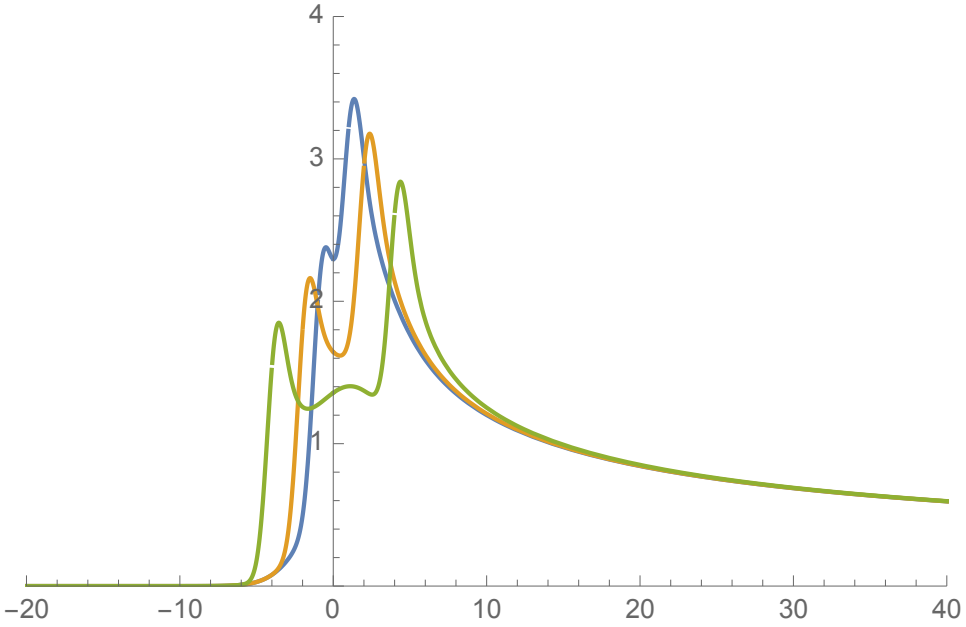

Figure 6: SAR altimeter waveform for significant wave height H_s = 4m and swell height H_{swell} = 2 (blue), 4 (tan) and 8m (green).

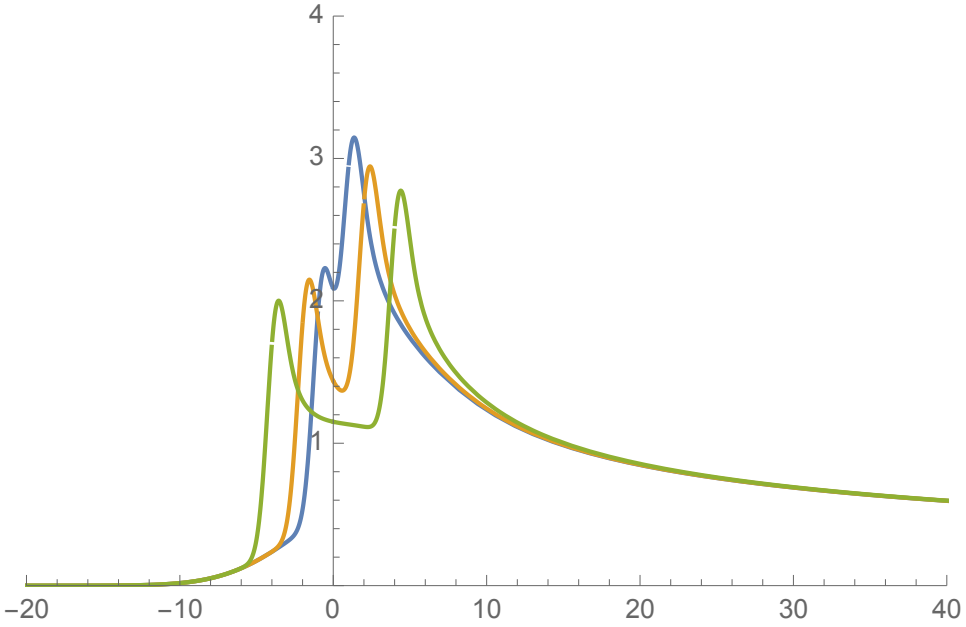

Figure 7: SAR altimeter waveform for significant wave height H_s = 8m and swell height H_{swell} = 2 (blue), 4 (tan) and 8m (green).

3.4. THE SPECIAL CASE OF SWELL CRESTS PARALLEL/QUASI-PARALLEL TO THE SAR ALTIMETER FOOTPRINT

To begin to understand what is happening consider the following very simple argument: in the parallel case (just as in the non-parallel case considered above) there will be reflection of the radar signal from the swell crests and troughs so it might be expected that the waveform will have a double peaked structure, or triple peaked if you add in a background sea component.

The key issue will be the number of crests and troughs in the footprint (see Figure 1) and that will depend on the ratio (λ/d) and the exact position of the SAR altimeter footprint relative to the swell crests and troughs. As both the SAR altimeter and the swell are moving this will change with time but for now assume a static picture (the effect of motion will be discussed later).

Consider the following simple cases (see Figure 1):

(a) $d/2 < \lambda < d$ => 2 crests and 1 trough OR 2 troughs and 1 crest

(b) $d < \lambda < 2d$ => 1 crest and 1 trough

given $d = O(300m)$ and $100m < \lambda < 400m$ approximately. If the strength of the return is equal for a crest and a trough (it may not be, but this assumption is made here for illustrative purposes only) then in case (a) with 2 crests and 1 trough, this would lead to a twice as much reflected power in the waveform at delays associated with the crests as with the trough, and vice versa for the 2 troughs and 1 crest scenario. In contrast, in case (b) with 1 crest and 1 trough, the peaks in the waveform would be of identical magnitude. The key point to note is that the waveform would have a similar double peaked structure to that found for the non-parallel geometry. This is consistent with the conclusions from the numerical simulations of Moreau et al. (2013) too.

3.5. EFFECT OF SWELL VELOCITY ON SAR ALTIMETRY

The SAR altimeter will be on a satellite with a footprint that is typically travelling at a ground speed $v \sim 7$ km s-1, while the swell waves with wavelengths 100-400m will have phase speeds $c_{phase} \sim 12.5$-25m s-1. The swell waves are therefore travelling much more slowly than the satellite footprint. Nevertheless, since SAR altimeter waveforms are built from the Doppler stack accumulated over SAR dwell times of a few seconds, the horizontal velocity of the swell waves could introduce a small amount of along-track smearing. Similarly, the vertical component of the swell orbital velocity could introduce small Doppler shifts that could cause mis-registration along-track and further waveform smearing. In both cases however, these effects are likely to be significant only for energetic long swell travelling parallel to the satellite track (i.e. crests parallel to the altimeter footprint). In the dataset examined in this study (see Section 4.2.5), swell travelling parallel to the satellite track with dominant wave height larger than 3 metres represent just 2% of the total dataset.

3.6. EFFECT OF SWELL WAVELENGTH ON SAR ALTIMETRY

The key question unanswered by the above analysis is: what is the swell wavelength dependence of the SAR altimeter return from the sea surface? The numerical simulation results of Moreau et al. (2013) suggest that there is a wavelength dependence but, as noted above, those numerical simulations assumed swell with heights of 12m and 16m for a wavelength of 100m, which is physically unrealistic. Therefore, the effect of swell wavelength on the SAR altimeter waveform remains an open question.

3.7. CONCLUSIONS ON THEORETICAL CONSIDERATIONS

Though the geometrical arguments and theoretical analysis presented here are somewhat simplistic, they serve to describe the various possible effects of swell on the SAR altimeter. Namely, they show that the presence of swell could lead to double or triple peaked SAR altimeter waveforms if the swell height is sufficiently large (see Figure 4 - Figure 7). The results suggest however that swell effects may not be detectable in SAR altimeter waveforms for swell less than ~2m in height. The analysis here confirms the behaviour seen from the small number of numerical simulations presented by Moreau et al. (2013).

The results also suggest that the double or triple peaked appearance of waveforms could be present irrespective of the wavelength of the swell waves, again, if the swell height is large enough. The theoretical approach adopted here does not allow investigation of any wavelength dependence, which probably would require numerical simulations of SAR altimeter processing with appropriately modelled speckle applied to explicit sea surfaces with moving swell. Even if this were possible, it would involve considerable computational effort without guarantee of indisputable conclusions.

The outstanding question that remains therefore is to what degree will such swell effects lead to biases in the retrieval of geophysical parameters from SAR altimeter waveforms, and if so, where and how frequently? These are the questions that we now try to address with empirical investigations of Cryosat-2 SAR altimeter, guided by the lines of enquiry suggested by our theoretical considerations.

4. EMPIRICAL INVESTIGATIONS OF SWELL EFFECTS IN CRYOSAT-2 SAR MODE

4.1. OVERVIEW

This activity extends the preliminary analyses of the effect of swell on SAR altimetry presented by Gommenginger et al. (2013b) using Cryosat-2 L1B SAR waveforms in the Central Atlantic and North-West European shelf. Swell conditions are characterised using satellite measurements of dominant swell wavelength, dominant swell height and dominant swell direction from the Envisat side-looking Advanced Synthetic Aperture Radar (ASAR) instrument, available from the GlobWave project (http://globwave.ifremer.fr/).

After collocating Cryosat-2 and Envisat ASAR, the assembled Cryosat-2/ASAR dataset is split into different swell categories according to ASAR swell wavelength, swell height and swell direction. The aim is to examine the Cryosat-2 SAR data under different swell conditions in order to detect possible waveform distortions and impact on L2 SSH that can be attributed to swell. Conversely, the approach seeks to characterise the type of swell conditions when an impact is discernable, so as to assess where and how often SAR altimetry data may be impacted by swell.

The same swell-categorisation approach is applied to three types of Cryosat-2 SAR mode products to explore different aspects of the problem:

- We begin by examining waveform shape in different swell conditions using operational ESA Cryosat-2 L1B SAR products. The aim is to determine the possible existence of waveform distortions (e.g. double peaks, smearing) in certain swell conditions.
- The same approach is then applied to L1B SAR waveforms obtained with the SARvatore processor to determine the role of L0-to-L1 processing. Unlike the ESA operational processor, which seeks to address the prime objectives of the Cryosat-2 mission for sea ice, the SARVatore processor has been optimised to process SAR altimeter waveforms over the ocean. The result is sharper waveforms that are better able to resolve small scale variability, and may consequently be more prone to swell effects.
- Finally, the possible impact of swell is examined with Cryosat-2 L2 SSH data, comparing SAR SSH against Pseudo-LRM SSH (P-LRM) in different swell conditions. In this analysis, it is assumed that P-LRM is not sensitive to swell (in the same way as LRM is supposedly unaffected by swell) and can be used as a baseline against which to assess SAR SSH results in different swell conditions.

4.2. DATASETS, COLLOCATION AND SWELL CONDITIONS

4.2.1. AVAILABLE DATASETS

Figure 8 presents the time span of various datasets available for use at the beginning of this study, showing the availability of different types of Cryosat-2 L1B and L2 products and of supporting ocean wave data.

The figure shows how the Cryosat-2 and the Envisat ASAR missions only overlap between April 2010 and April 2012. With Cryosat data available from July 2010 and Envisat end-of-life being declared in early May 2012, the period of interest for this study is therefore July 2010-May 2012.

Other sources of ocean wave data include output from the WaveWatch3 model (WW3; available for example from Ifremer) and L2 swell products from the Copernicus Sentinel-1 (S-1) side-looking SAR. These have not been considered so far in the study: S-1 L2 swell products only started to become available close to the end of this project and were not used in this study. Similarly, WW3 output was not used, partly because of ongoing uncertainties about wave models' ability to accurately represent swell (and particularly swell direction), partly in order to focus available efforts on the assessment against Envisat ASAR.

Cryosat-2 L1B SAR waveform data consist of the operational ESA L1B products, available continuously since July 2010. So far, ESA L1B products have been produced with three ground-processing versions, known as Baseline A, B and C, over different periods of the Cryosat-2 mission. In this study, we avoid possible differences between the different ESA processed products by limiting the analyses to Baseline B products, which represent the largest consistent dataset available for the 2010-2012 period of interest at the start of this study.

One year of CNES Cryosat Pilot Products (CPP) is available through collaboration with the ESA SCOOP project. The CNES CPP use L0 to L1B processing that is optimised for SAR altimetry over the ocean, and deliver sharper more accurate waveforms that those from the operational ESA processor. However, the CNES CPP dataset is limited to the period Nov 2013 to Oct 2014, and thus provides no overlap with Envisat ASAR.

Finally, Cryosat-2 SAR data reprocessed with the ESA SARvatore processor was made available to the study courtesy of Salvatore Dinardo. Like CPP, the SARvatore processor optimises L0-to-L1 processing for SAR altimeter waveforms over the ocean. It also retracks waveforms to L2 with the SAMOSA model that is being used in the operational processor for Sentinel-3. The SARvatore products provide 20Hz waveforms as well as L2 retrieved altimeter measurements at 20Hz and 1Hz and various geophysical corrections and ancillary data. The products were made available only for those Cryosat-2 tracks that are known to have collocated data with Envisat ASAR.

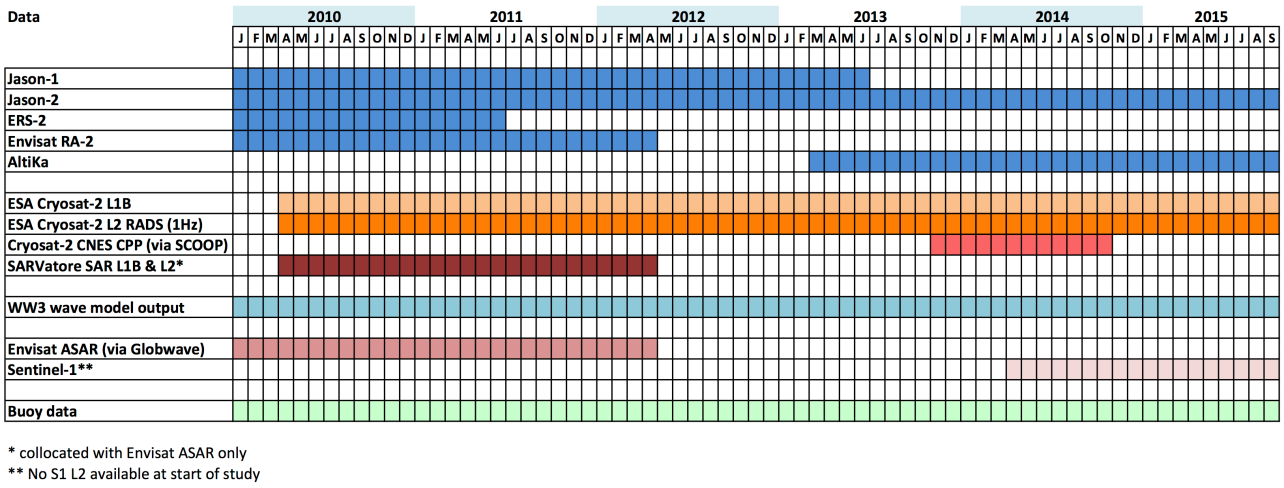

Figure 8: Time span of different Cryosat-2 products and supporting ocean swell data.

4.2.2. CRYOSAT-2 COLLOCATION WITH ENVISAT ASAR

Figure 9 shows the geographical distribution of Cryosat-2 SAR mode data in March 2012. The Cryosat-2 SAR mode mask during this period was version 3.2, corresponding to the Cryosat-2 acquisition plan used between April 2011 and April 2012. A large Cryosat-2 SAR mode box became available in the central Pacific from May 2012 (mask version 3.3), but narrowly missed providing any overlap with Envisat, which ended in April 2012. The study focuses on Cryosat-2 SAR mode data in the central South Atlantic, the Agulhas region and the North-East Atlantic in order to avoid regions of typically low sea state (Indonesia, Mediterranean Sea) or that could be contaminated by sea ice.

Globwave Envisat ASAR data has global coverage and provides estimates of wave height, dominant wavelength and wave direction for the dominant and the second dominant swell train. It should be noted that side-looking SAR do not resolve the full ocean wave spectrum because of azimuth cut-off of high-frequency waves linked to the motion of the waves during SAR imaging (Stopa et al., 2015b). Hence, side-looking SAR only resolve ocean waves longer than approximately 150-200 metres depending on sea state, and the wave height, length and direction provided by Envisat ASAR relate to swell waves only. Separate swell trains are identified using spectral partitioning as part of the ASAR L2 processing. We focus mainly on the dominant swell, which is identified by its higher wave height.

Globwave ASAR data were extracted for regions that coincide with Cryosat-2 SAR mode acquisitions (Figure 10) and were collocated with Cryosat-2 L1B SAR mode data. Although the central Pacific box is shown in Figure 10, it turns out that there is no Cryosat-2 data in that box during the lifetime of Envisat.

Collocation between Cryosat-2 SAR altimetry and Envisat ASAR swell measurements consists of collocating Cryosat-2 SAR L1B waveforms at 20Hz within a 300 km radius limit and 24 hours of the ASAR data. These collocation parameters may a-priori seem unusually

broad but reflect the fact that swell conditions tend to change slowly spatially and temporally (e.g. compared to wind). As always, the choice of space-time collocation criteria is the result of a trade-off between ensuring the data is representative of conditions across that space-time interval, and securing a high-enough number of samples to enable statistical analyses.

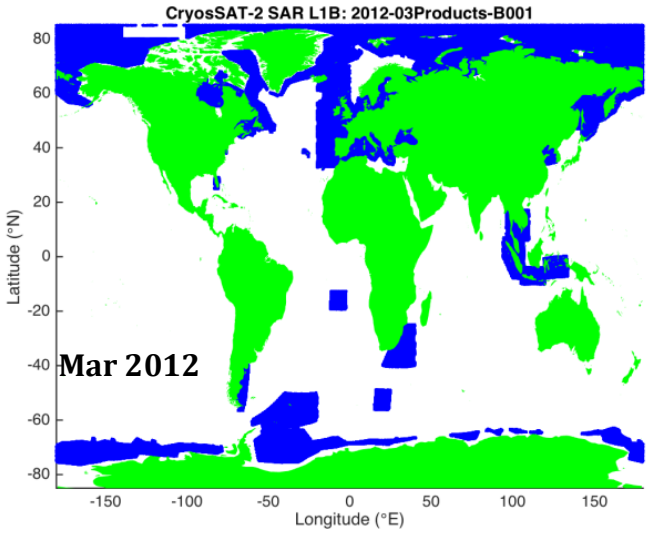

Figure 9: Geographical location of Cryosat-2 L1B SAR mode data in March 2012.

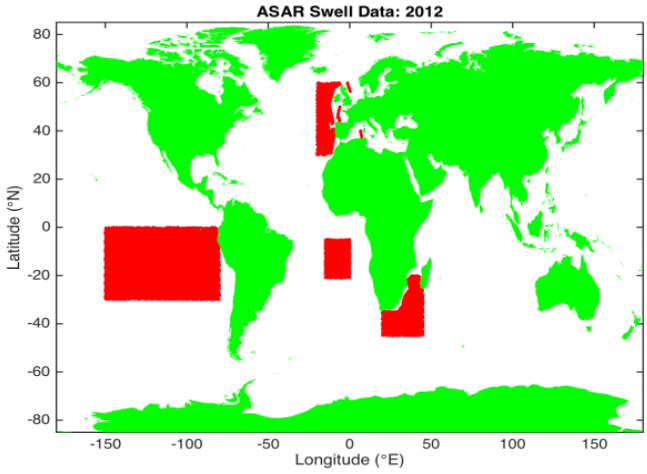

Figure 10: Regions selected for extraction of Globwave Envisat ASAR swell data in 2012.

Occasionally, the Cryosat-2 waveforms can be collocated with several separate ASAR acquisitions within the selected space-time separation criteria, in which case we chose the ASAR data located closest in space and time to the Cryosat-2 data.

Conversely, each ASAR acquisition will usually be collocated with several Cryosat-2 20Hz waveforms. In some cases, we examine the single Cryosat-2 20Hz waveform located closest to the ASAR measurement, but because single 20Hz waveforms are subject to speckle noise, we also retain the 100 Cryosat-2 waveforms located closest to ASAR.

4.2.3. SWELL CONDITIONS IN COLLOCATED DATASET

Maps of the dominant and second dominant swell wavelengths for January-April 2012 are shown in Figure 11 in the large central Pacific box, the NE Atlantic box, the Agulhas box and the central South Atlantic box. The dominant and second dominant swell wave trains are identified in order of decreasing swell significant wave height. The two bottom subplots in Figure 11 show only swell wavelengths greater than 400m.

The swell wavelengths reported in the ASAR products range from 40 to 680 m. Long swell cases (> 400m) are mainly found in the open ocean box in the central Pacific, with smaller number of occurrences in the central Atlantic, the Agulhas region and the NE Atlantic.

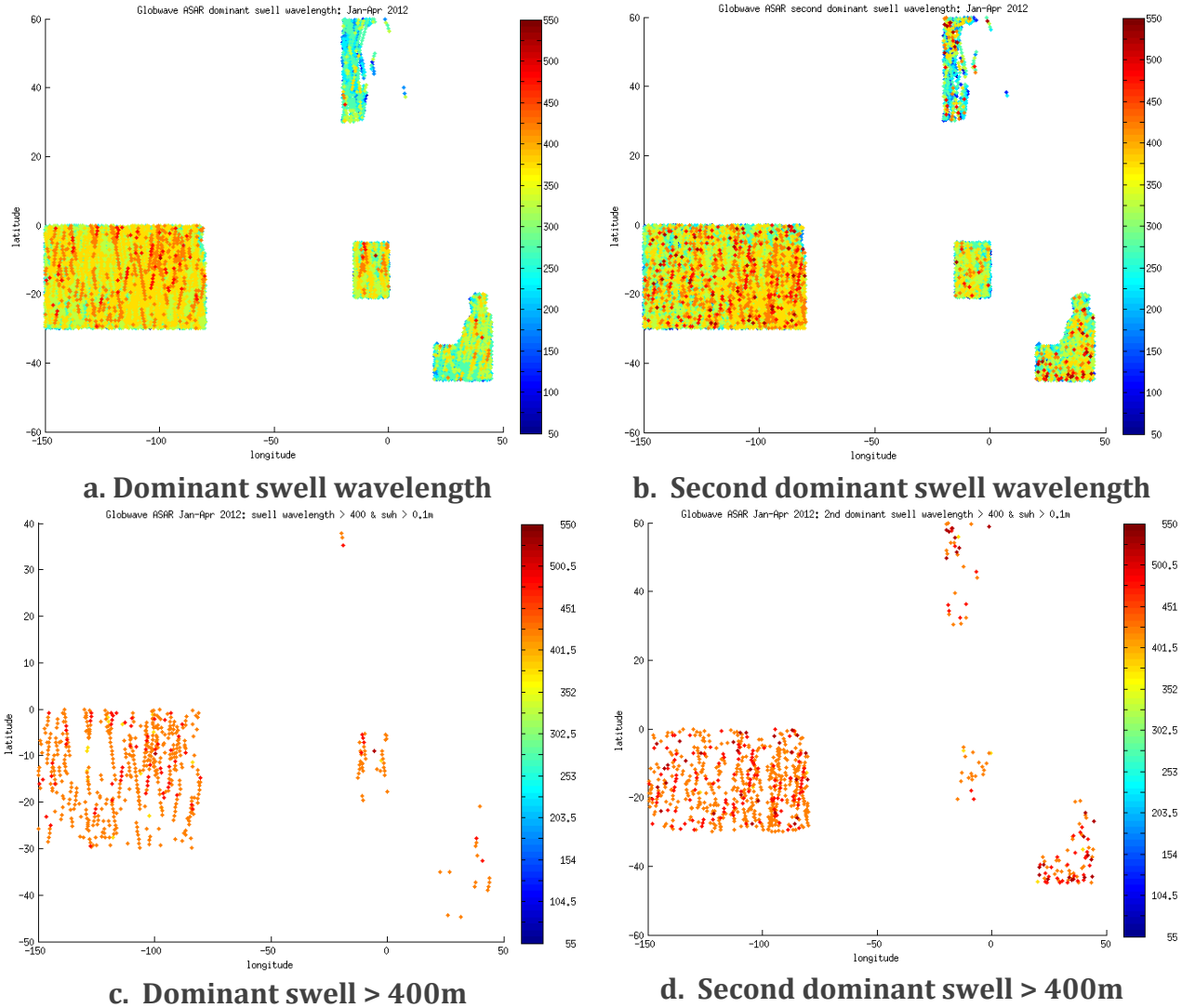

a. Dominant swell wavelength

b. Second dominant swell wavelength

c. Dominant swell > 400m

d. Second dominant swell > 400m

Figure 11: Map of dominant (a, c) and second dominant (b, d) swell, for all significant wave heights over 0.1m, where colour denotes the swell wavelength. Figures a and b show all swell between January-April 2012. Figures c and d show only swell with wavelength over 400m. Colour axis limits range from 55m and 550m

Figure 12 shows the distributions of swell wavelengths and swell wave heights as histograms. Dominant swell length is typically between 250 to 350 m, with fewer data with swell lengths below 200 m or more that 400 m. By comparison, the second dominant swell length has more occurrences of shorter (100 to 200 m) and longer (> 400 m) wavelengths.

The dominant swell wave height ranges between 0 and 6.4m, with values typically around 1 m. The wave height of the second dominant swell is typically lower, with value around 0.5 m. These results are consistent with expected distributions of swell characteristics in these regions.

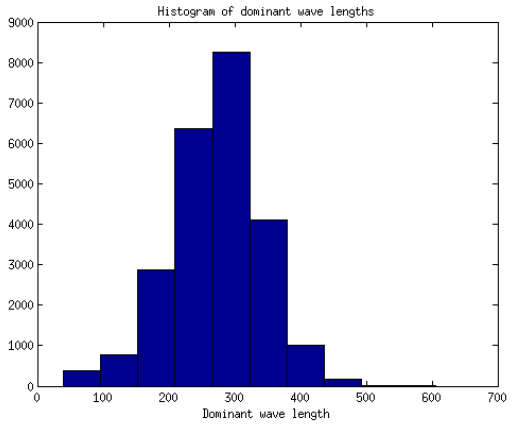

a. Dominant swell length 2012

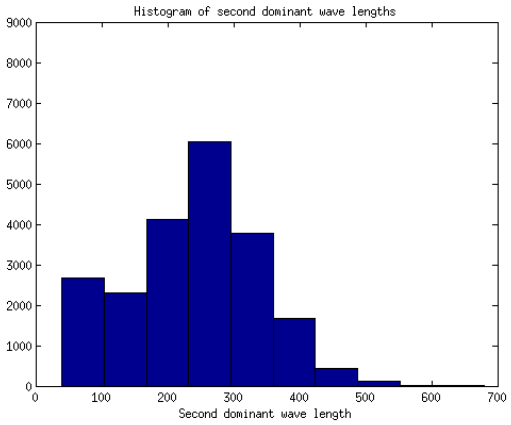

b. Second dominant swell length 2012

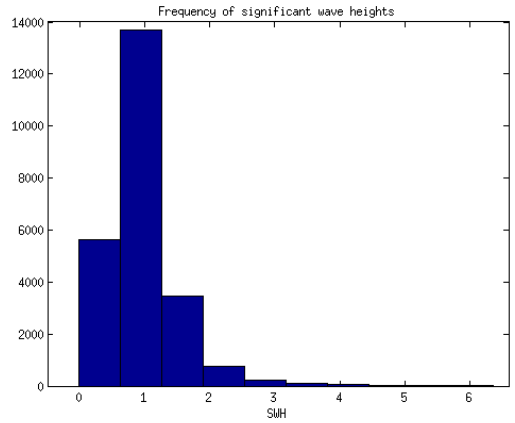

c. Dominant swell height 2012

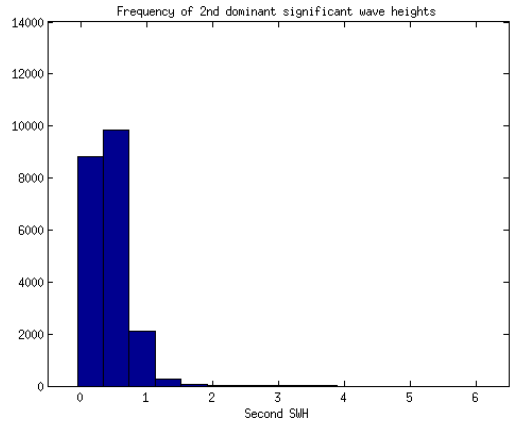

d. Second dominant swell height 2012

Figure 12: Histograms of (a) dominant swell length, (b) second dominant swell length, (c) dominant swell height and (d) second dominant swell height in Globwave ASAR data collocated with Cryosat-2 SAR data for 2012.

Figure 13 plots the direction, height and wavelength of the dominant swell for the full collocated dataset. We note that there are many more swell waves travelling in the East-West direction (direction = 90 and 270 deg) than in the North-South direction (direction = 0 or 180

deg). This is particularly true for swell waves longer than 300 metres wavelength, which travel almost predominantly eastwards (i.e direction = 90 deg) with the exception of a very few cases of long northward travelling swell.

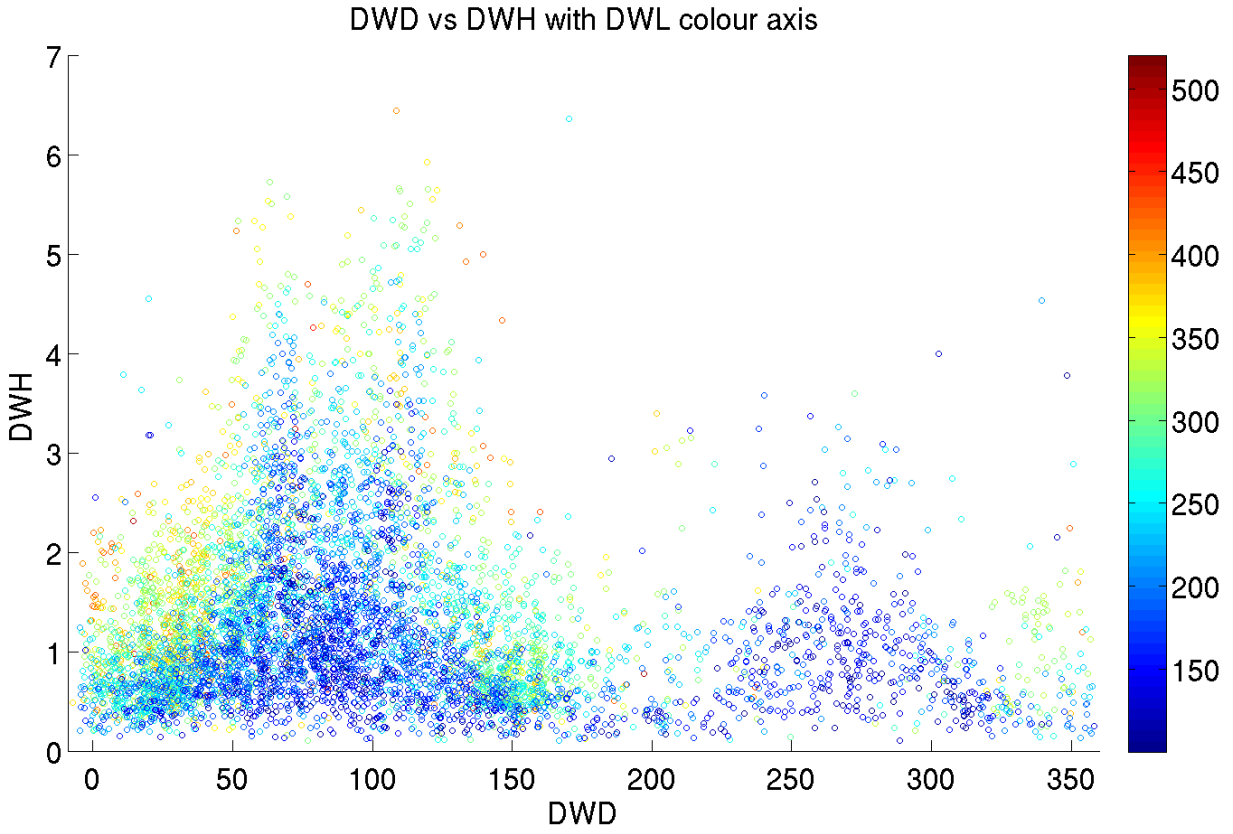

Figure 13: Dominant swell direction against dominant swell height with dominant swell length shown by the colour scale. The data correspond to the full Envisat ASAR/Cryosat-2 SAR collocated dataset. Dominant swell direction" represents the direction of propagation of the dominant swell system as reported in the Envisat ASAR products.

4.2.4. PARALLEL & PERPENDICULAR SWELL RELATIVE TO CRYOSAT-2 TRACKS

Cryosat-2 has an inclination of 92 degrees from the equator (Cryosat-2 product handbook 2012) when it is ascending, or travelling northwards (88 degrees from the equator when descending, or travelling southwards). In the South Atlantic box, this results in tracks aligned in a direction close to North-South. An example of the direction of Cryosat-2 ascending and descending tracks is shown in Figure 14.

The Cryosat-2 track orientation is used with the ASAR dominant wave direction to compute the relative direction of the swell to the Cryosat-2 ground-track. The relative direction is not calculated exactly for ascending and descending tracks, but rather, is used to determine whether the swell direction is parallel, perpendicular or oblique to the altimeter track.

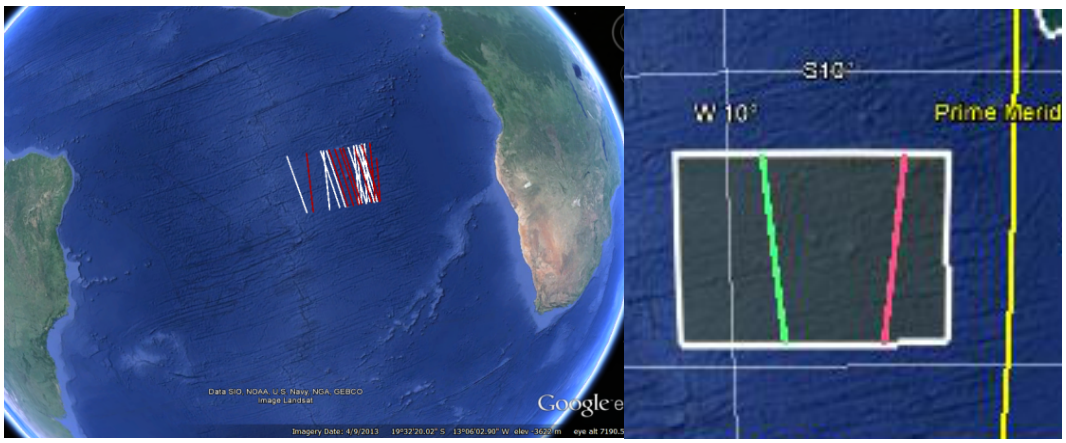

Figure 14: An example of Cryosat-2 tracks in the South Atlantic box showing (left) Cryosat-2 tracks for dominant swell wavelengths between 100-200 m in red and 400+ m swell in white. (right) the direction with regards to North of Cryosat-2 ascending (green) and descending (pink) ground tracks.

The terminology "parallel" and "perpendicular" will be used extensively in this study and refers to the alignment of the ocean swell propagation to the altimeter track (or, similarly, the alignment of the swell crests with the SAR altimeter asymmetric footprint). The geometrical configuration that correspond to these terms is illustrated in Figure 15.

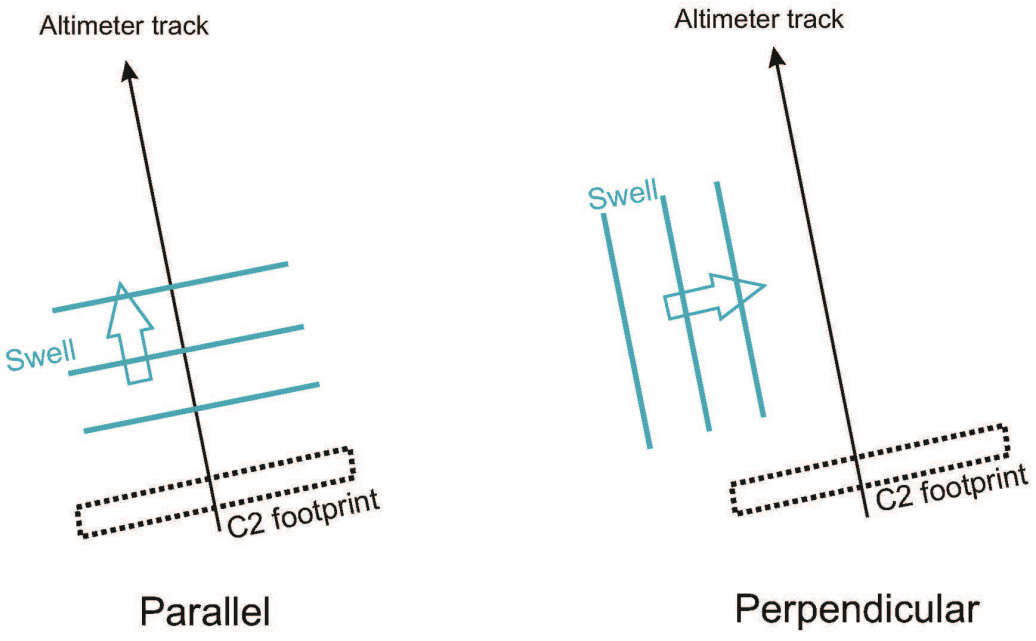

Figure 15: Geometrical configuration of the swell and the Cryosat-2 track for cases referred to as "parallel" and "perpendicular".

The implications for swell orientation vis-à-vis Cryosat-2 tracks is shown in Figure 16. With Globwave ASAR swell direction provided in degrees from North (Globwave D.7 PUG3

v1.0), swell will be considered perfectly parallel with the altimeter track when its direction is 358 degrees or 178 degrees for ascending tracks, and 2 degrees or 182 degrees for descending tracks. Similarly, swell will be considered exactly perpendicular with the altimeter track when its direction is 268 degrees or 88 degrees for ascending tracks, and 272 degrees or 92 degrees for descending tracks.

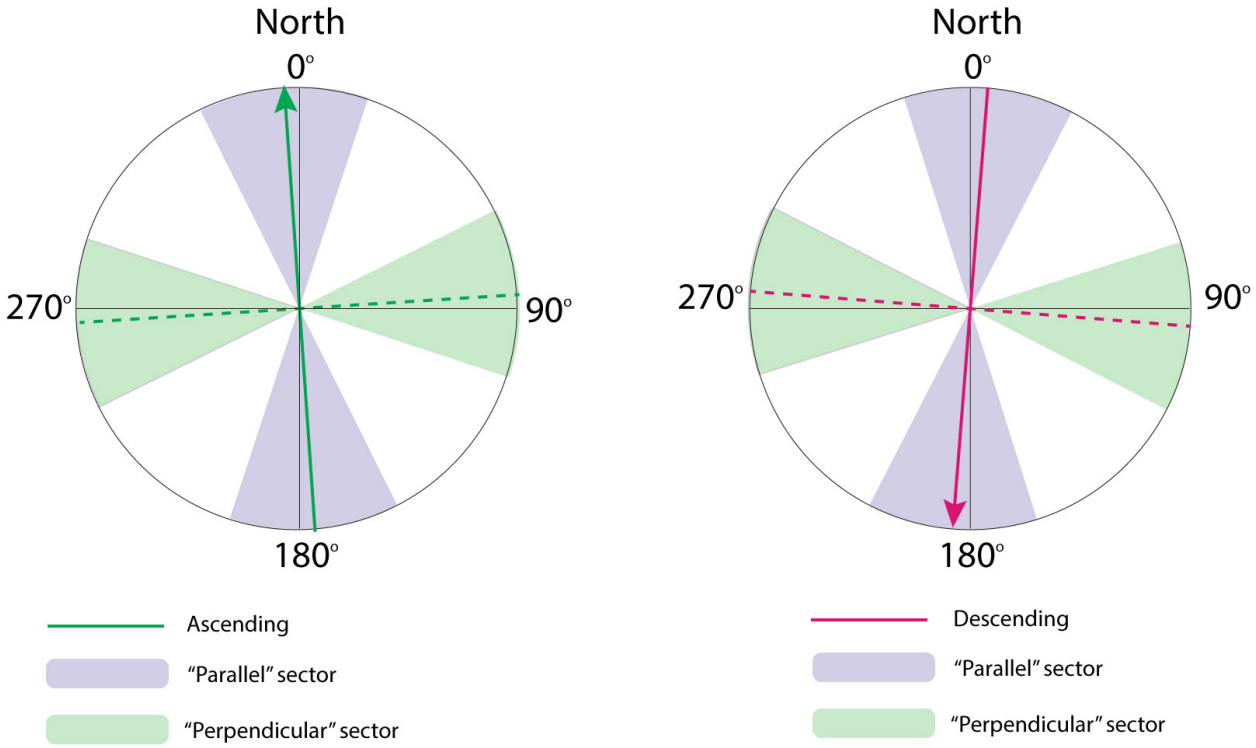

Figure 16: Swell orientation vis-à-vis Cryosat-2 ascending and descending tracks.

Since there will be only a small number of cases where swell will be oriented exactly in the parallel or perpendicular direction, swell will be categorised as "parallel" or "perpendicular" when they fall within a certain angle of the exact parallel and perpendicular directions. In this study, swell were categorised as "parallel" or "perpendicular" when travelling within +/- 22.5 degrees of the exact parallel or perpendicular directions, although some investigations were also performed with narrower angular sectors of +/- 5 degrees. Any swell falling outside the parallel or perpendicular angular sectors will be referred to as "other" or "oblique". The angular sectors that correspond to parallel and perpendicular swell for ascending and descending tracks are shown in Figure 16.

4.2.5. SWELL ORIENTATION IN THE COLLOCATED DATASET

Figure 17 shows the composition of the collocated dataset in terms of ASAR dominant swell height, length and orientation. On both suplots, the ASAR swell data are plotted against total significant wave height obtained from the collocated Cryosat-2 Pseudo-LRM data available via RADS (http://rads.tudelft.nl/rads).

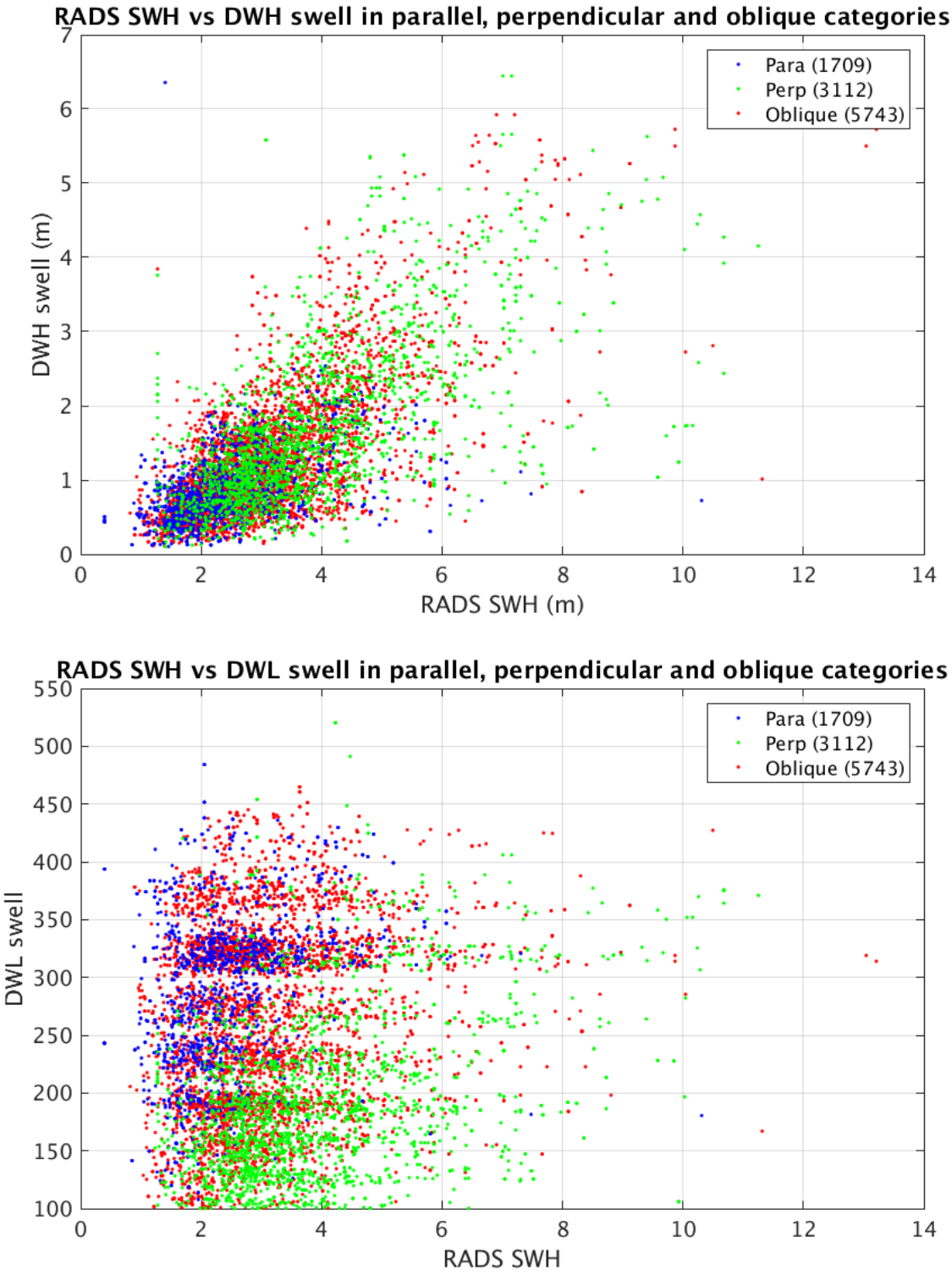

Figure 17: ASAR dominant swell (top) height (bottom) length against total significant wave height from Cryosat-2 PLRM (via RADS) with colours referring to parallel, perpendicular and oblique swell categories. Swell is considered "Parallel" or "Perpendicular" when propagating within ±22.5º of the direction parallel or perpendicular to the track, and "Oblique" elsewhere.

We note the following:

- Oblique is the dominant category, with 54% (5743) of the total number of points (10564); perpendicular is the next most populated category with 29% (3112) of the dataset; finally, parallel is the least frequently encountered case, representing just 16% (1709) of the collocated dataset.
- Perpendicular swell (green points in Figure 17) can reach large values of wave height and wavelength, and have a distribution that is very similar to the "oblique" category.
- Parallel swell (blue points) span the full range of swell wavelengths, with a tendency towards swell longer than 300 metres, but the parallel swell height is almost always less than 2 metres.

Finally, Figure 18 shows the geographical distribution of the data obtained in different swell categories. There is no apparent systematic geographical bias in the occurrence of particular swell categories. The only exception is the South Atlantic box, which features no cases of perpendicular swell. This last point is surprising and being investigated further for verification purposes.

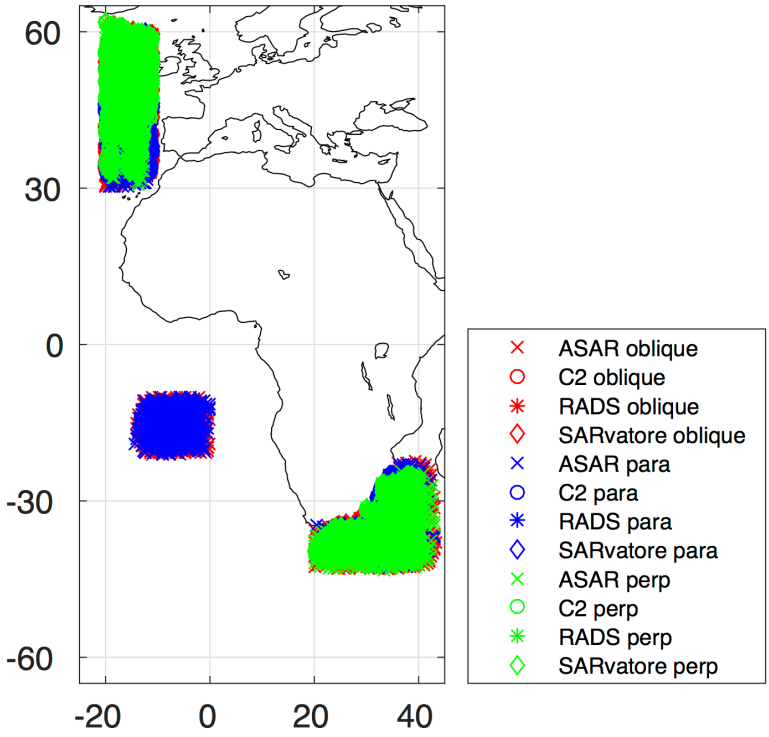

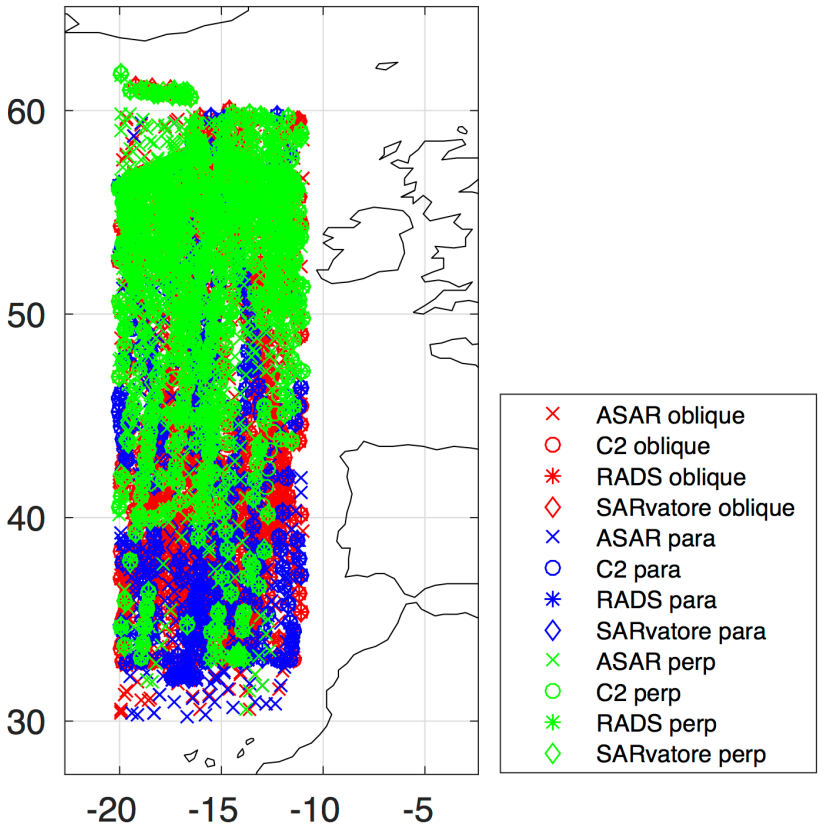

Figure 18: Geographical location of the collocated dataset showing Envisat ASAR (crosses), ESA operational Cryosat-2 SAR mode (circles), RADS 1Hz (stars) and Cryosat-2 SAR mode from the SARvatore processor. Colours correspond to swell orientation category "Oblique" (red), Parallel (blue) and perpendicular (green). Right plot shows zoomed-up view of the North-East Atlantic box.

4.3. WAVEFORM SHAPE ANALYSES WITH ESA CRYOSAT-2 L1B DATA

4.3.1. FIRST RESULTS WITH SINGLE 20HZ WAVEFORMS

Figure 19 and Figure 20 show two pairs of 20Hz waveforms obtained in the same region on the same ground track with similar swell wave height and relative direction to the track, but different dominant swell wavelengths. In Figure 19a and Figure 20a, swell wavelengths are within 100-200 m, while in Figure 19b and Figure 20b, swell wavelengths are 400+ m.

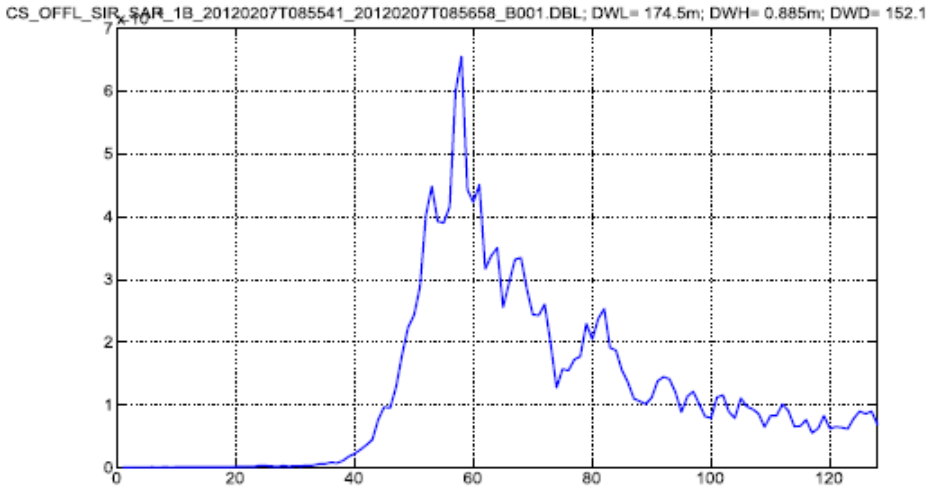

Dominant Wavelength (DWL) = 174m

Dominant Wave Height (DWH) = 0.88m

Dominant Wave Direction (DWD) = 152°

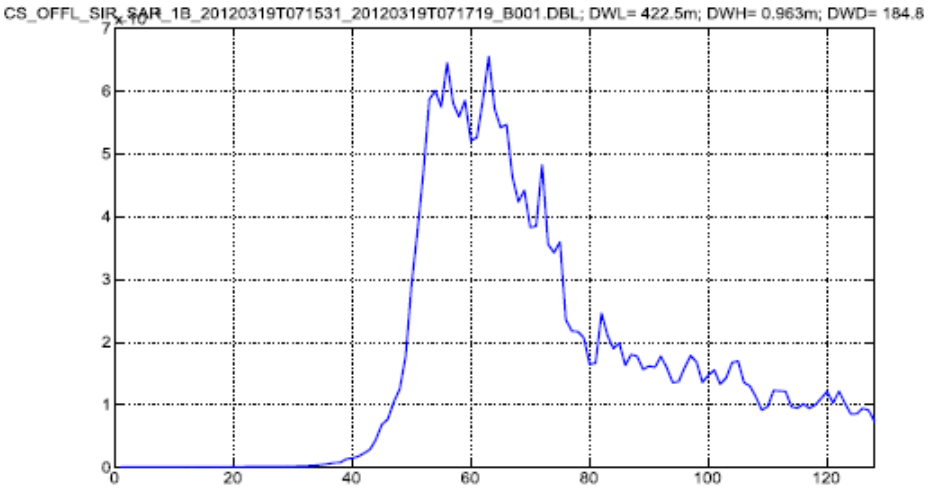

Dominant Wavelength (DWL) = 422m

Dominant Wave Height (DWH) = 0.96m

Dominant Wave Direction (DWD) = 185°

Figure 19: Two Cryosat-2 SAR mode 20Hz waveforms from the same region, same ground track, same swell height and similar swell direction but different swell wavelength of (a) 100-200 m and (b) 400+ m. In both (a) and (b) wave direction is parallel to the altimeter track.

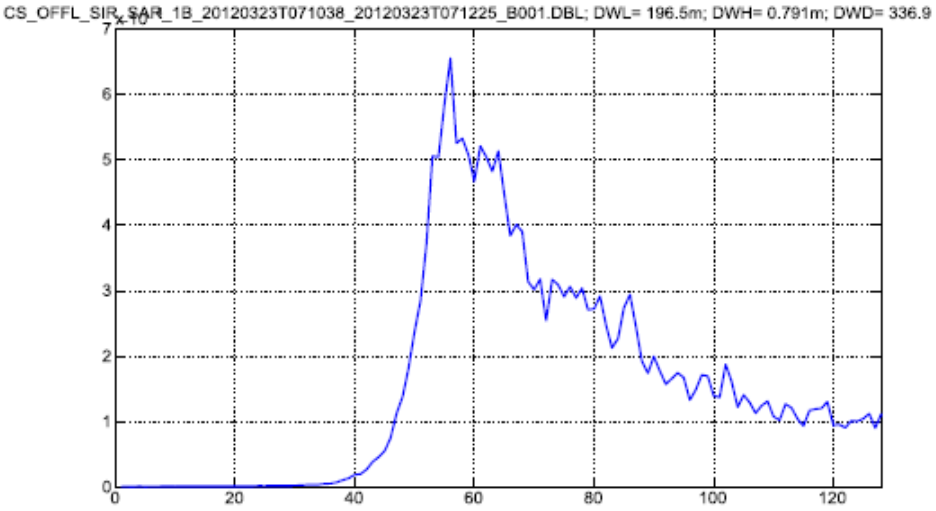

Dominant Wavelength (DWL) = 196 m

Dominant Wave Height (DWH) = 0.79 m

Dominant Wave Direction (DWD) = 337°

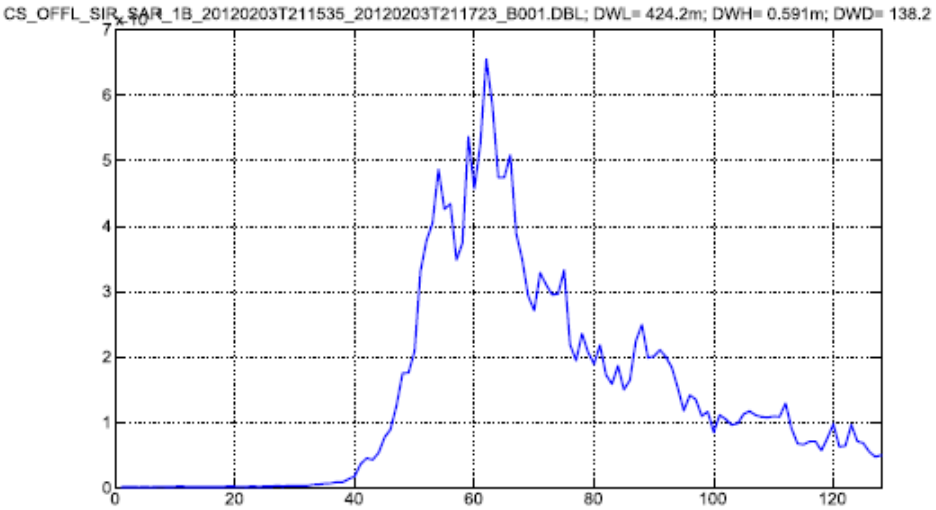

Dominant Wavelength (DWL) = 424 m

Dominant Wave Height (DWH) = 0.59m

Dominant Wave Direction (DWD) = 138°

Figure 20: Two Cryosat-2 SAR mode 20Hz waveforms from the same region, same ground track, same swell height and similar (modulo 180) swell direction but different swell wavelength of (a) 100-200 m and (b) 400+ m. In both (a) and (b) wave direction is perpendicular to the altimeter track.

These first results suggest possible distortions of the waveforms, particularly in the case of longer swell, which hint at the presence of multiple peaks. However, as 20Hz waveforms can be affected by anomalies and speckle, it is not possible to be conclusive on the basis of these two examples. Analyses need to be extended to a larger dataset to confirm statistically whether these are one-off anomalies or whether these features are robust across different datasets in the presence of swell.

As mentioned above, in some cases, one ASAR acquisition can collocate with several Cryosat-2 passes within the 300km/24-hour separation window used for co-location. In Figure 21, waveforms that all collocate with a specific Globwave ASAR acquisition are plotted

together. Waveforms plotted in red are single 20Hz waveforms that correspond to conditions where dominant swell wavelength is 432 m, dominant wave height is 2.17 m and swell direction is 36 degrees. Shown in blue are two 20Hz waveforms corresponding to conditions where dominant swell wavelength is 420 m, dominant wave height is 0.56 m and dominant wave direction is 146.9 degrees. As can be seen, there is a reasonable level of consistency between the waveforms in each group, which display similar shape and features. This type of analysis will be repeated hereafter using multi-waveform averages to provide more conclusive results.

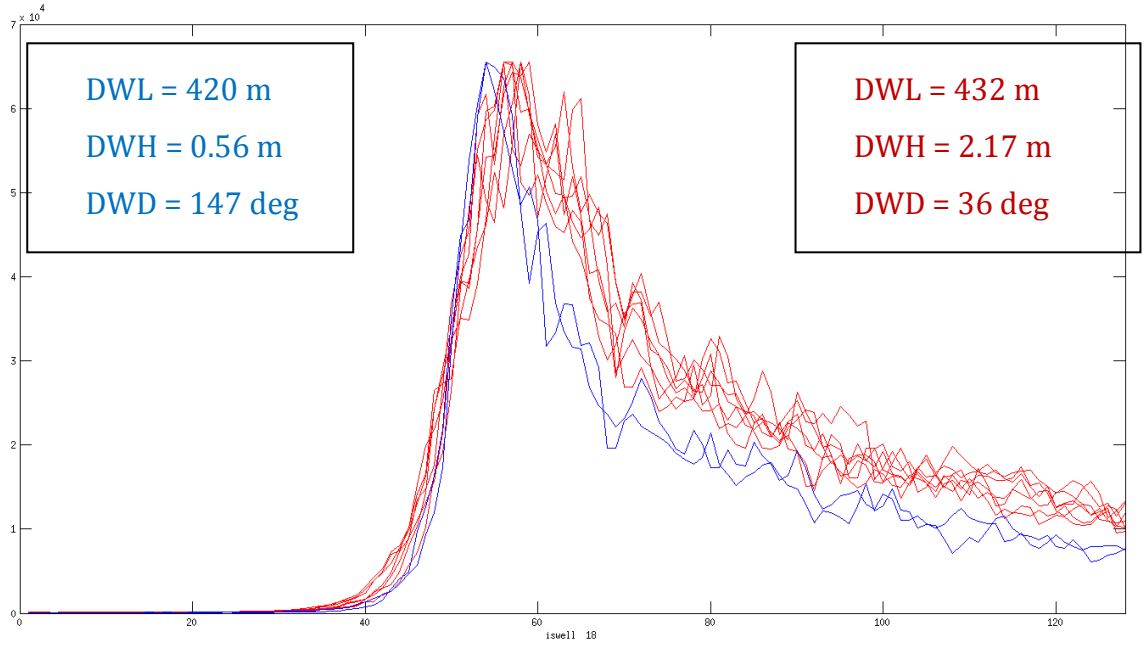

Figure 21: Waveforms from similar conditions overlain to assess their similarity.

4.3.2. AVERAGE WAVEFORMS

For each collocation, the hundred (100) 20Hz Cryosat-2 SAR waveforms located closest to the ASAR measurement are extracted. Here, we use along-track averaging over the block of 100 waveforms to produce average and standard deviation waveforms. The average and standard deviation waveforms are simply built by calculating the mean and standard deviation of the 100 waveforms in each bin. Two examples of average waveforms are shown in Figure 22 for two different swell cases. The title shows the Cryosat-2 filename, the separation distance from Envisat ASAR and the altimeter direction of travel. The legends give the characteristics of the dominant swell conditions.

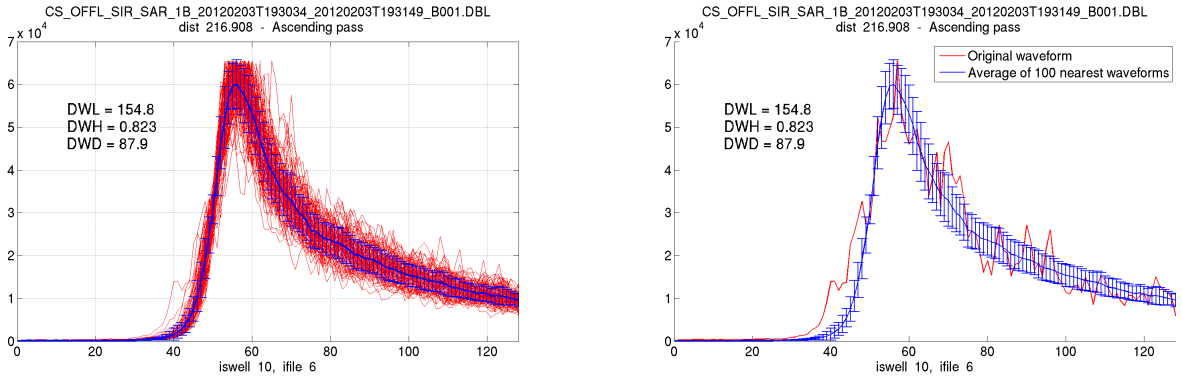

Dominant swell length within 100-200 metres

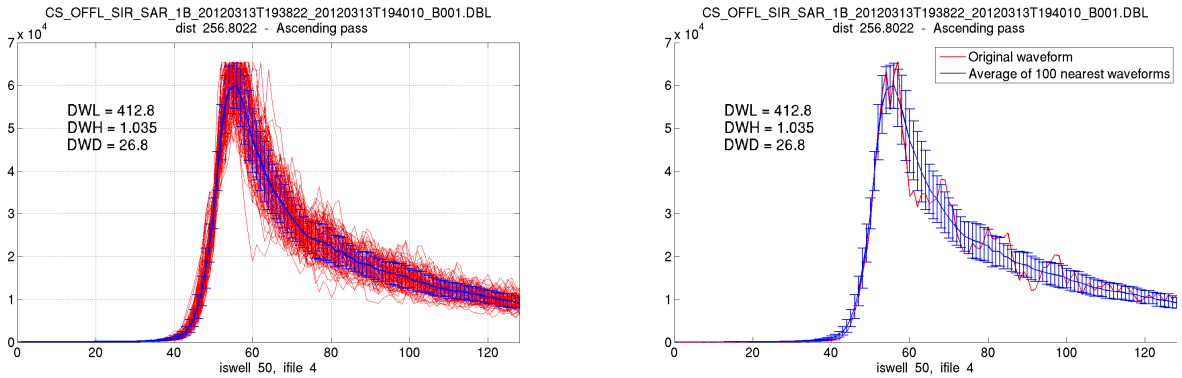

Dominant swell length 400+ metres

Figure 22: Cryosat-2 SAR waveforms collocated with Envisat ASAR shown (left, in red) as the 100 20Hz waveforms located closest to ASAR and (right, in blue) the average waveform with standard deviation. Top plots correspond dominant swell length within 100-200 metres, bottom plots correspond to dominant swell length of 400+ metres.

4.3.3. DEPENDENCE OF AVERAGE WAVEFORMS SHAPE ON SWELL PARAMETERS

Here, the average SAR waveforms contained in the collocated dataset are sorted in order of increasing swell height, swell length and swell direction to detect any tendency in the average and standard deviation waveform shape to change with different swell parameters.

Figure 23 and Figure 24 show respectively the average and standard deviation waveforms stacked along the x-axis in order of increasing swell height, swell length and swell direction. In each plot, the y-axis shows the 128 waveform bins with the peak located around bin 58.

The results confirm what we expect in terms of wave height, namely that the Cryosat-2 waveforms become broader and more variable with increasing swell wave height. The altimeter waveforms do in fact respond to the total significant wave height, but as seen previously (see Figure 17), the dominant swell wave height is generally well correlated with total significant wave height in this dataset.

In contrast, there is no apparent tendency with swell length, not in the average, nor in the standard deviation waveform.

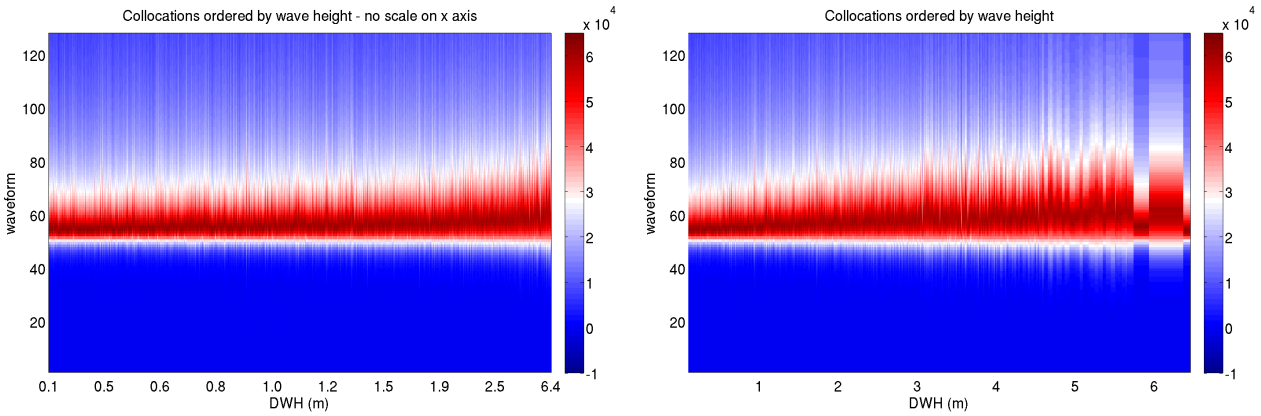

Average Cryosat-2 SAR waveforms ordered by dominant swell wave height

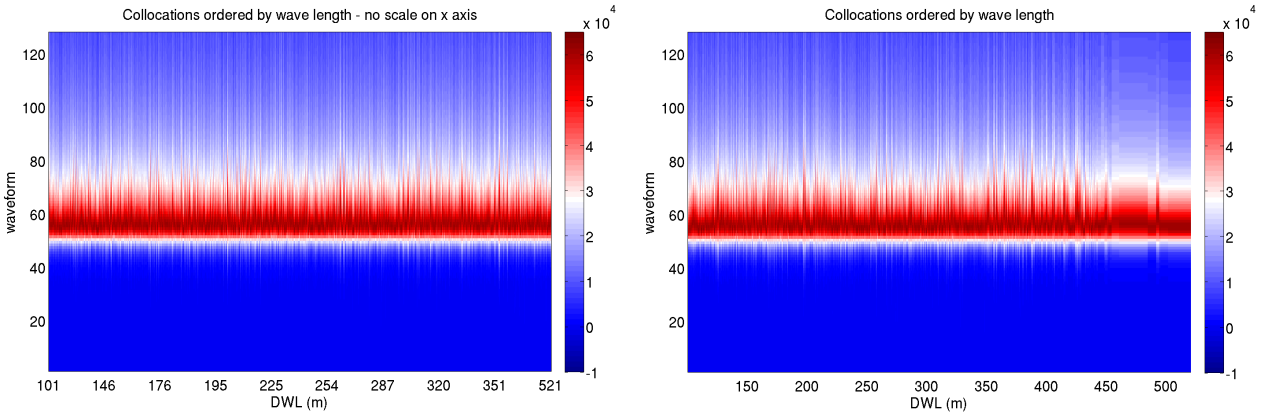

Average Cryosat-2 SAR waveforms ordered by dominant swell wave length

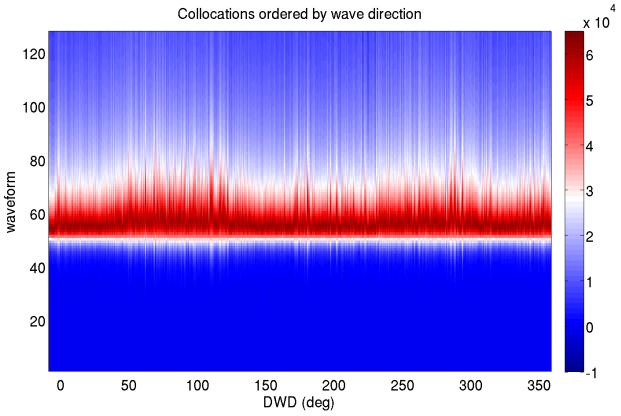

Average Cryosat-2 SAR waveforms ordered by dominant swell wave direction

Figure 23: Average Cryosat-2 SAR waveforms ordered by (top) dominant swell wave height (middle) dominant swell wave length (bottom) dominant swell direction. Left plots use irregularly spaced x-axes that depend on the composition of the collocated dataset; Right plots use x-axes with regular spacing.

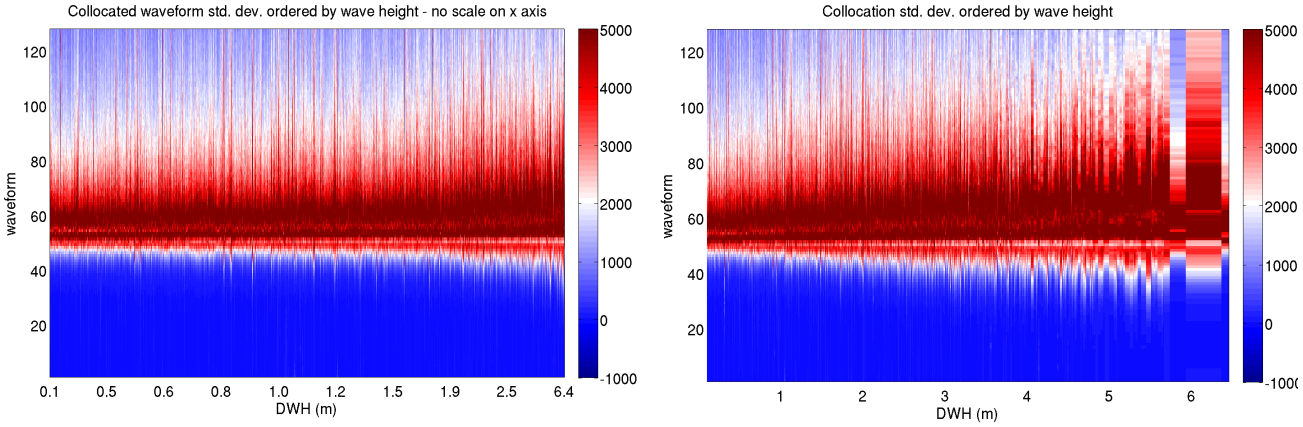

Standard deviation Cryosat-2 SAR waveforms ordered by dominant swell wave height

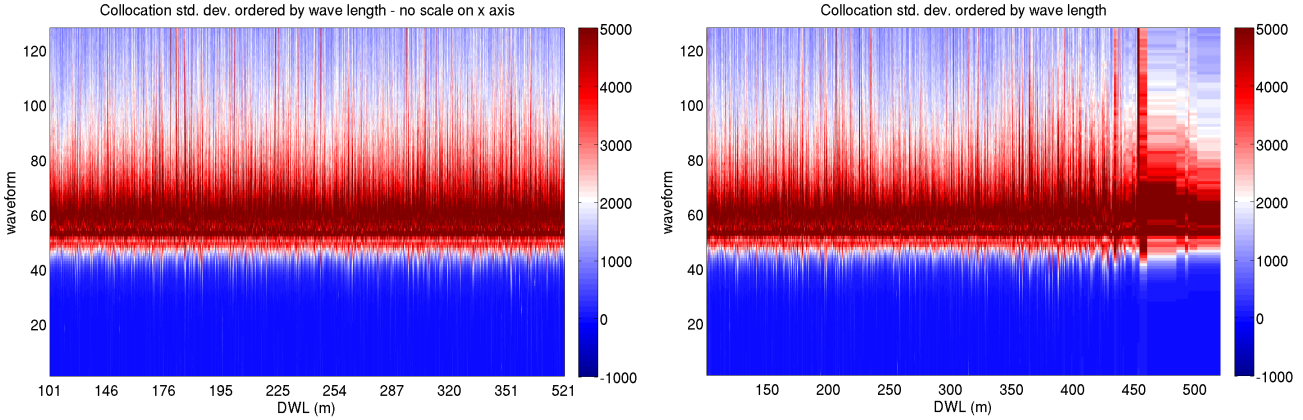

Standard deviation Cryosat-2 SAR waveforms ordered by dominant swell wave length

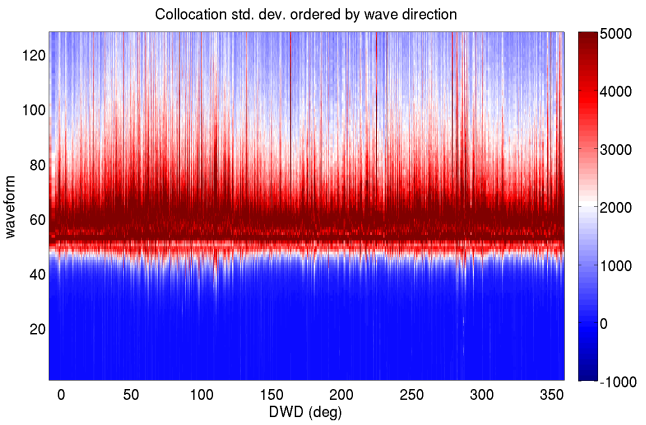

Standard deviation Cryosat-2 SAR waveforms ordered by dominant swell wave direction

Figure 24: Standard deviation Cryosat-2 SAR waveforms ordered by (top) dominant swell wave height (middle) dominant swell wave length (bottom) dominant swell direction. Left plots use irregularly spaced x-axes that depend on the composition of the collocated dataset; Right plots use x-axes with regular spacing.

We note however the striking pattern with swell direction, whereby average and standard deviation waveforms are broader for swell travelling in the East-West direction. This unexpected result becomes however rapidly understood when recalling the distribution shown in Figure 13, which indicated that swell from that sector also has typically larger wave height. The signature with swell direction seen in the SAR waveforms is therefore simply the mark of swell waves from East-West directions being generally more energetic.

4.3.4. MEAN WAVEFORM SHAPE FOR PARALLEL & PERPENDICULAR SWELL

Average Cryosat-1 SAR waveforms are now split into different swell wavelength and swell orientation categories. This is shown in Figure 25. In each plot, waveforms in the parallel category are shown in red, waveforms in the perpendicular category are shown in blue. The number of parallel and perpendicular cases is annotated on each subplot.

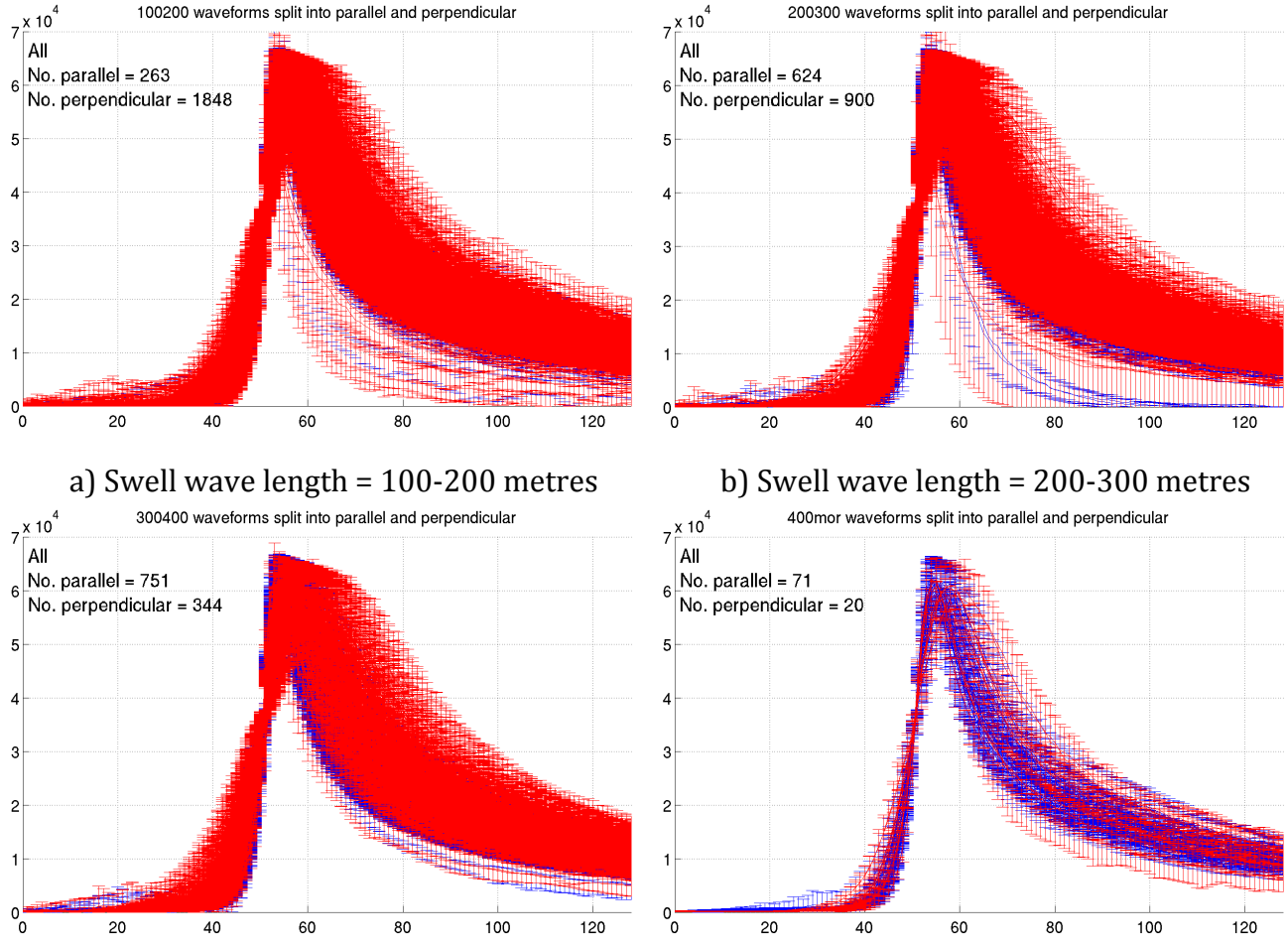

a) Swell wave length = 100-200 metres

b) Swell wave length = 200-300 metres

c) Swell wave length = 300-400 metres

d) Swell wave length = 400+ metres

Figure 25: Average Cryosat-1 SAR waveforms in different swell wavelength and swell orientation categories. Parallel shown in red, perpendicular shown in blue.

The average waveforms found in Figure 25 for each swell category are now further averaged to present one single mean waveform per swell length and parallel/perpendicular category. This is shown in Figure 26. There is no clear swell signature with swell length or direction, with mean parallel and perpendicular waveforms generally falling within one standard deviation of each other. The small differences that are observed are most likely caused by the different make-up of the data in each category, particularly in terms of significant wave height from different directional sectors.

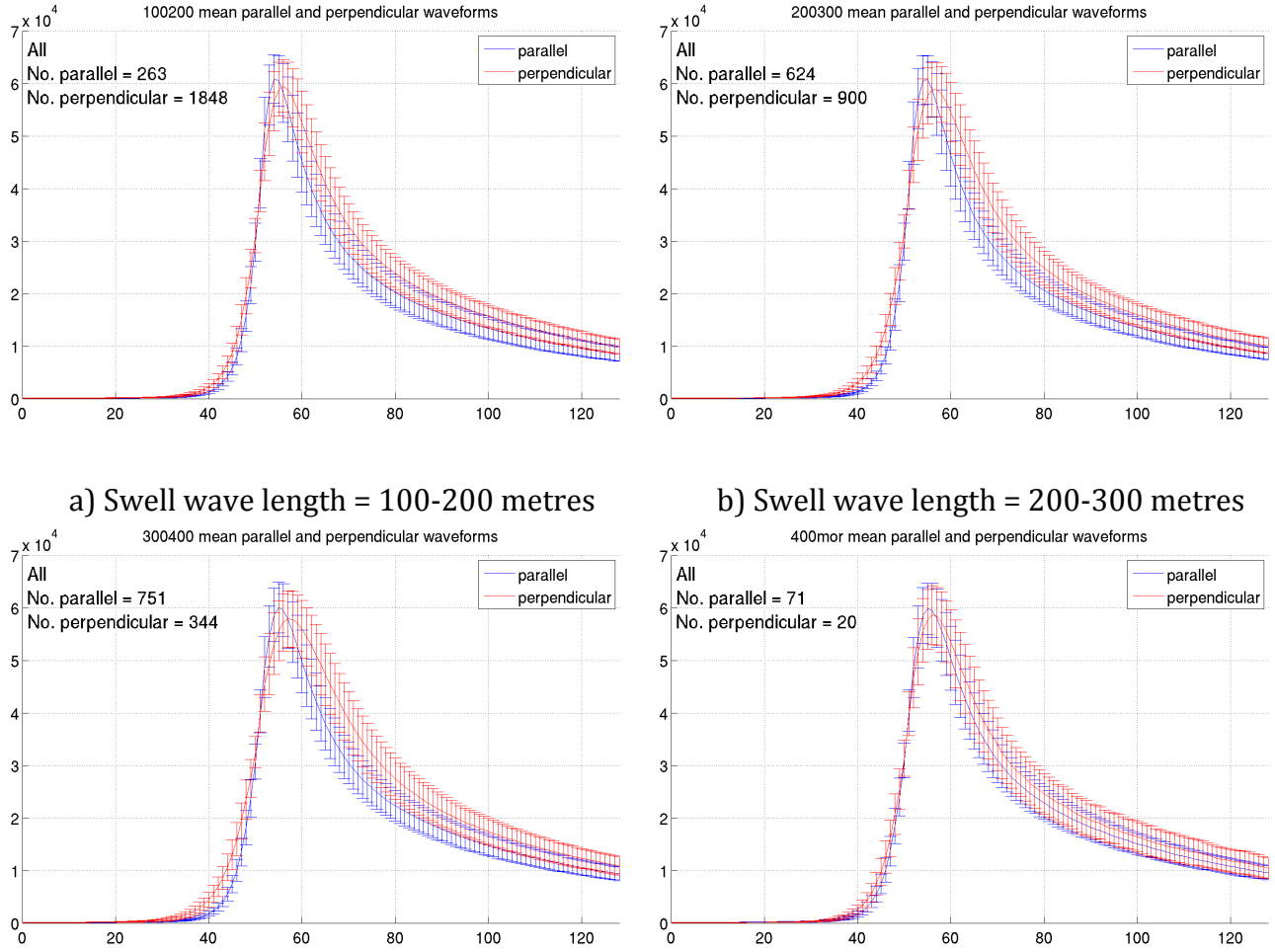

a) Swell wave length = 100-200 metres

b) Swell wave length = 200-300 metres

c) Swell wave length = 300-400 metres

d) Swell wave length = 400+ metres

Figure 26: Mean Cryosat-2 SAR waveforms for different swell length and swell orientation categories. Parallel cases shown in red, perpendicular in blue.

4.3.5. MEAN WAVEFORM SHAPE IN DIFFERENT SWELL CATEGORIES

This final set of plots considers the mean waveform shape obtained in different swell categories, but unlike the previous section, also accounts for some measure of wave height.

Figure 27 shows the mean waveforms for parallel, perpendicular and oblique swell orientation in different dominant swell height (down the rows) and dominant swell length (across the columns) categories. In each subplot, the number of samples in each category is indicated in the legend. The shading represents one standard deviation from the mean.

No significant difference or overall pattern with swell height, length or orientation is discernable. Occasionally, the parallel waveforms stand out in a few categories, but these correspond to cases with fewer than 25 separate occurrences, i.e. at least one order of magnitude fewer samples than in other categories, so that statistical significance of the difference cannot be assured.

Figure 27 used dominant swell height as a way of discriminating swell categories. However, bearing in mind that altimeter waveforms respond to total significant wave height rather than swell height, the same analysis is repeated with wave height taken as the total significant wave height obtained from collocated 1Hz RADS data. This is shown in Figure 28. The outcome is the same as for Figure 27, with no reliable evidence of any effect of swell on mean waveforms, other than the occasional oddity linked to the small number of samples in particular categories.

4.4. WAVEFORM SHAPE ANALYSES WITH SARVATORE CRYOSAT-2 L1B PRODUCTS

The mean waveform shape analysis presented in Figure 28 was repeated using Cryosat-2 20Hz waveforms from the SARvatore processor provided by Salvatore Dinardo.

As for the ESA operational products, the SARvatore waveforms data were collocated with Envisat ASAR to assign the Cryosat-2 SAR waveforms to different swell categories. The results are shown in Figure 29 using the same convention as in Figure 28.

We note the slightly peakier appearance of the mean waveforms in all swell categories compared to those obtained with the ESA operational products, which was expected. Other than that, there is no reliable evidence indicating swell effect on waveform shape in any swell categories.

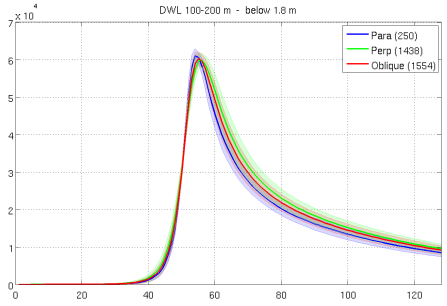

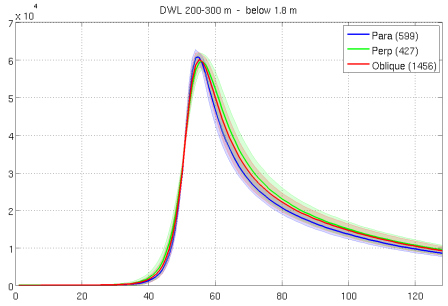

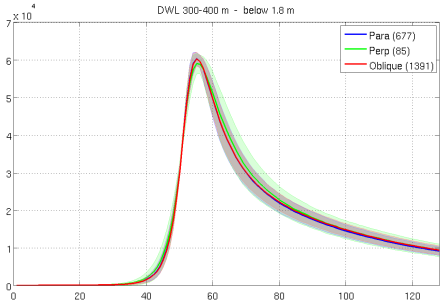

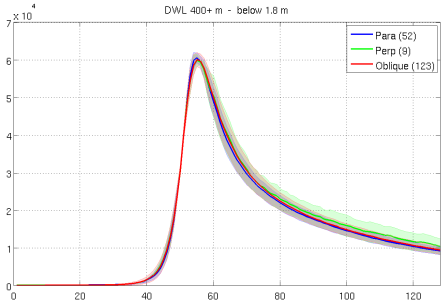

Dominant swell height below 1.8 m

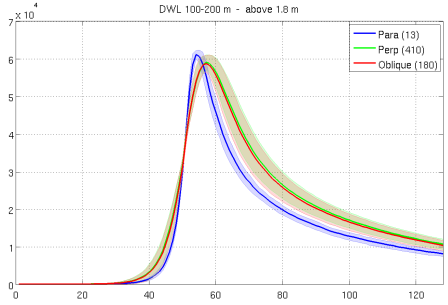

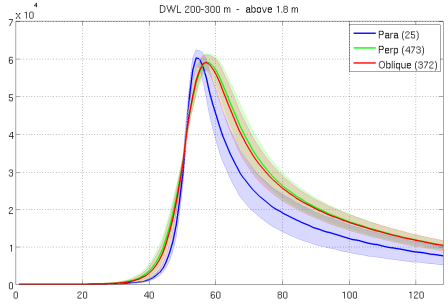

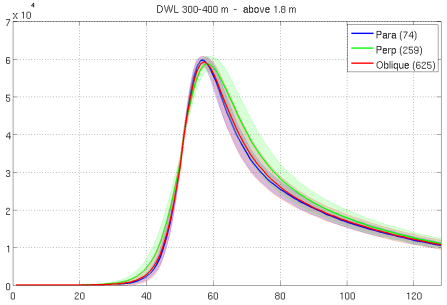

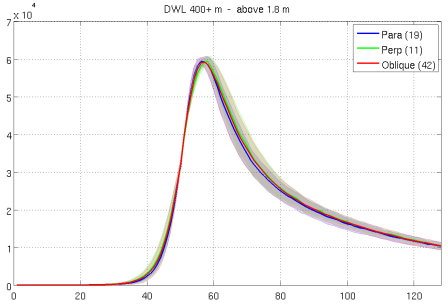

Dominant swell height above 1.8 m

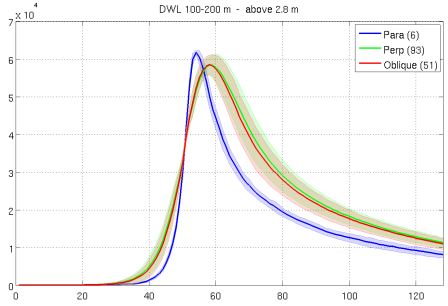

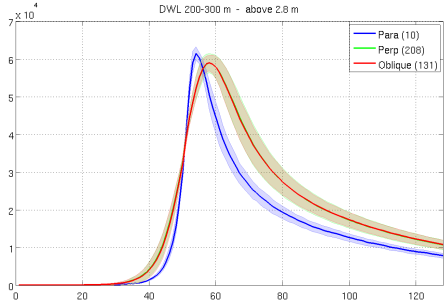

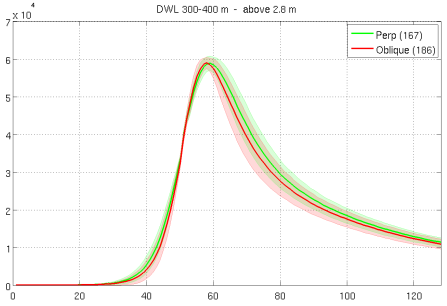

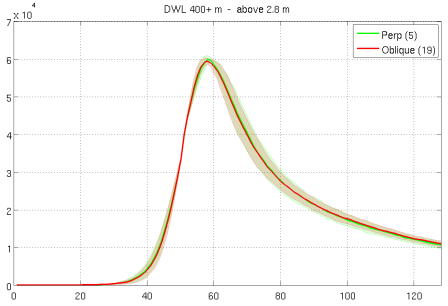

Dominant swell height above 2.8 m

(Caption on next page)

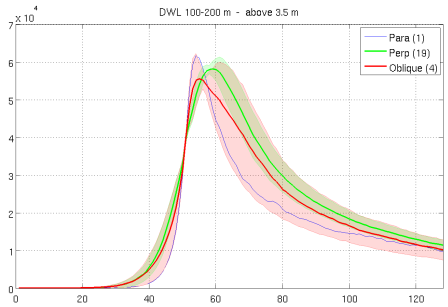

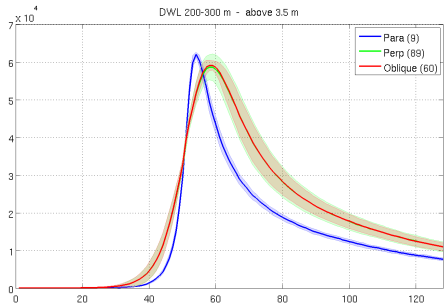

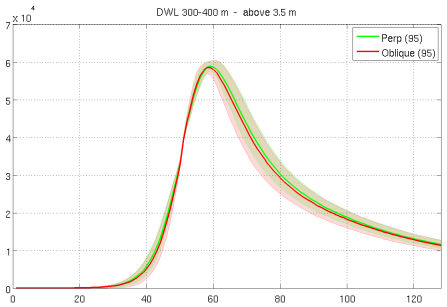

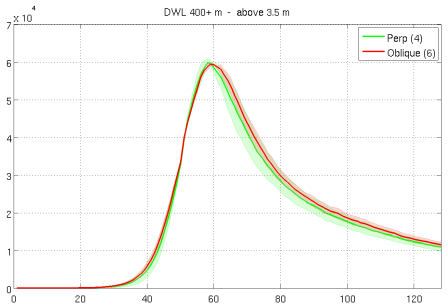

Dominant swell height above 3.5 m

No data

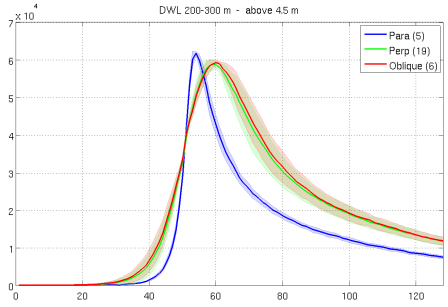

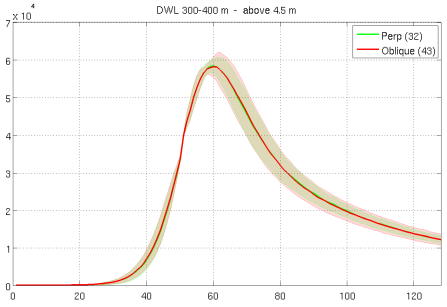

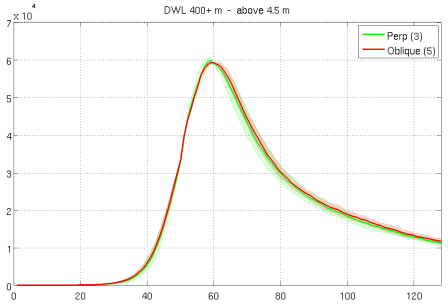

Dominant swell height above 4.5 m

Figure 27 (including previous page): Mean Cryosat-2 SAR waveforms in different categories of (rows) dominant swell height and (columns) dominant swell length for (blue) parallel, (green) perpendicular and (red) oblique swell orientation. The number of samples in each category is shown in the legend. The data shown are L1B waveforms obtained from the operational ESA Baseline B products.

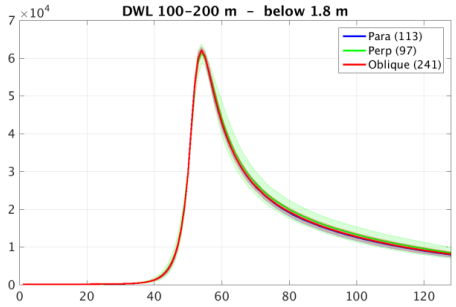

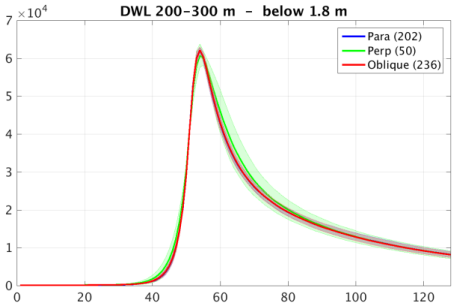

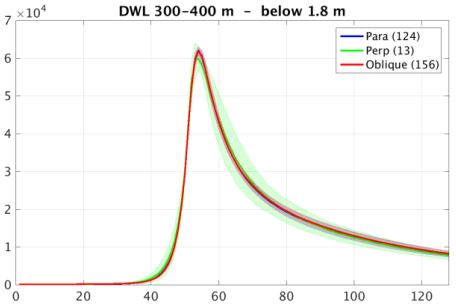

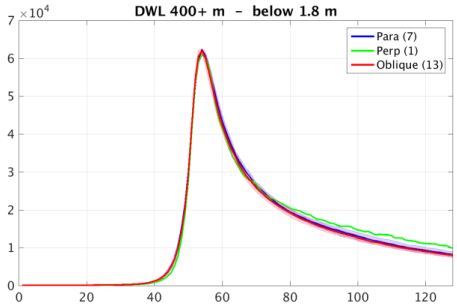

RADS Significant height below 1.8 m

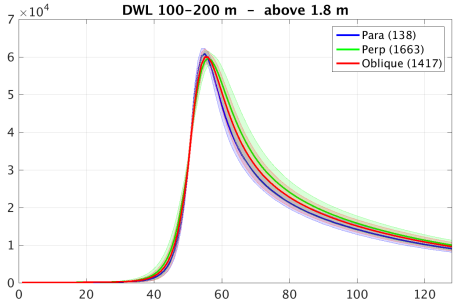

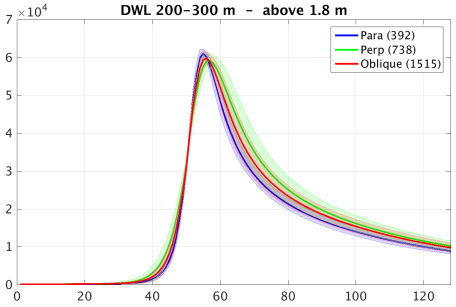

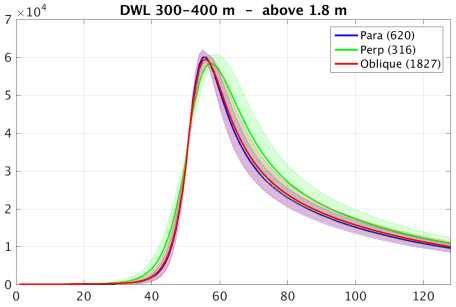

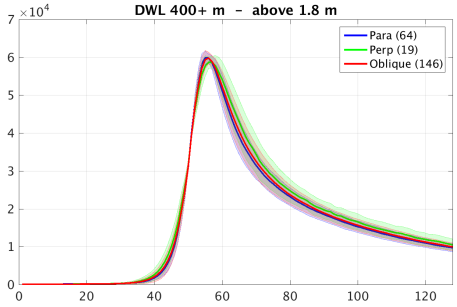

RADS Significant height above 1.8 m

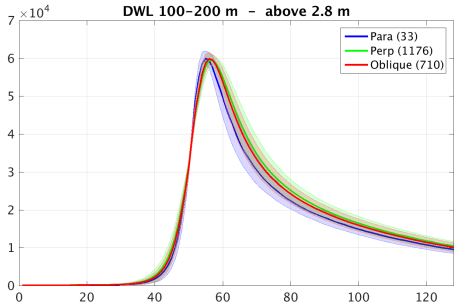

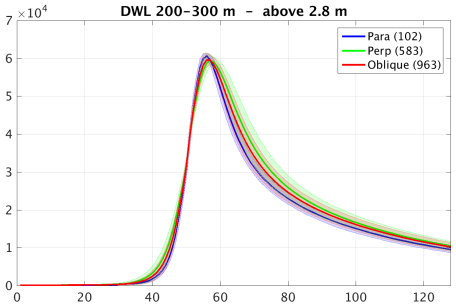

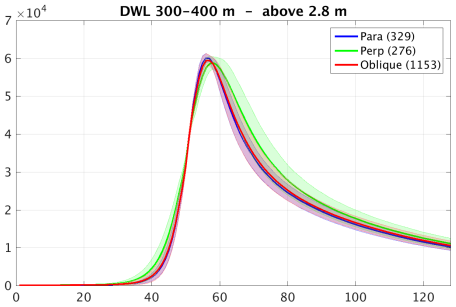

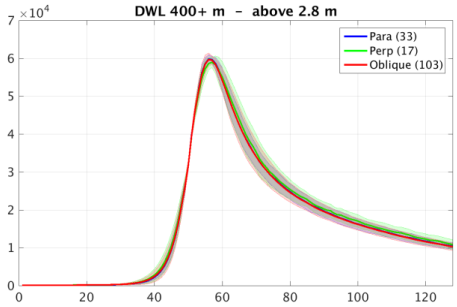

RADS Significant height above 2.8 m

(Caption on next page)

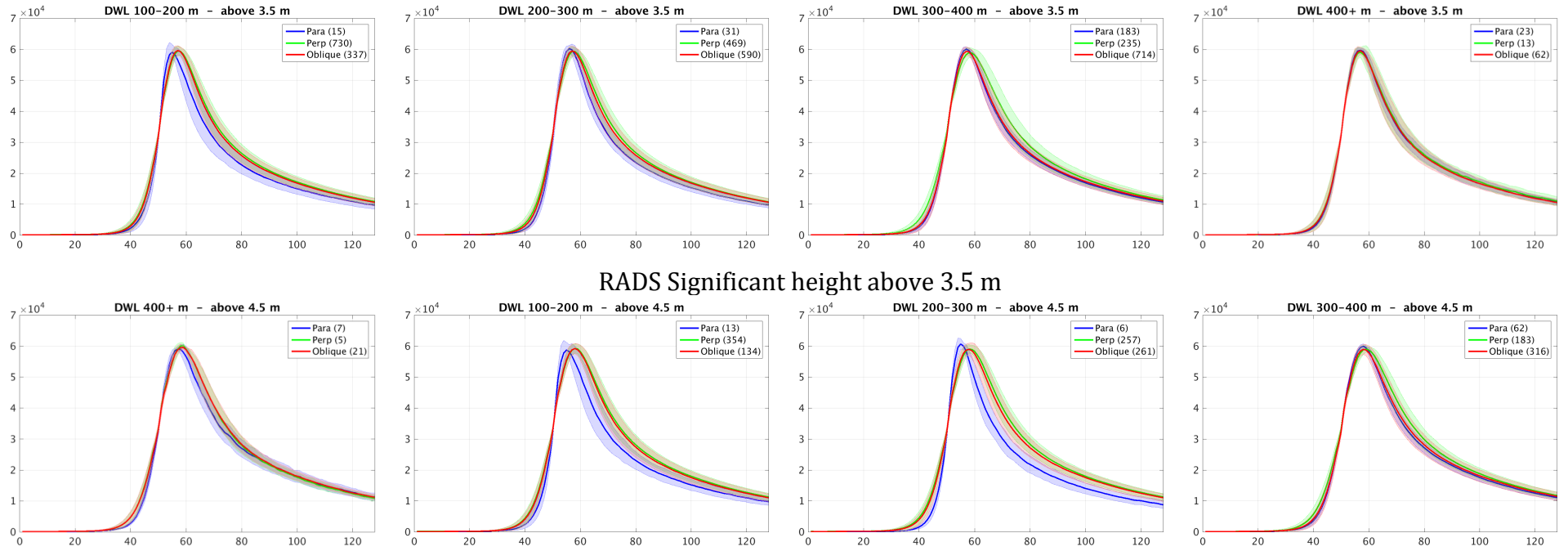

Figure 28 (including previous page): Mean Cryosat-2 SAR waveforms in different categories of (rows) dominant swell height and (columns) dominant swell length for (blue) parallel, (green) perpendicular and (red) oblique swell orientation. The number of samples in each category is shown in the legend. The data shown are L1B waveforms obtained from the operational ESA Baseline B products.

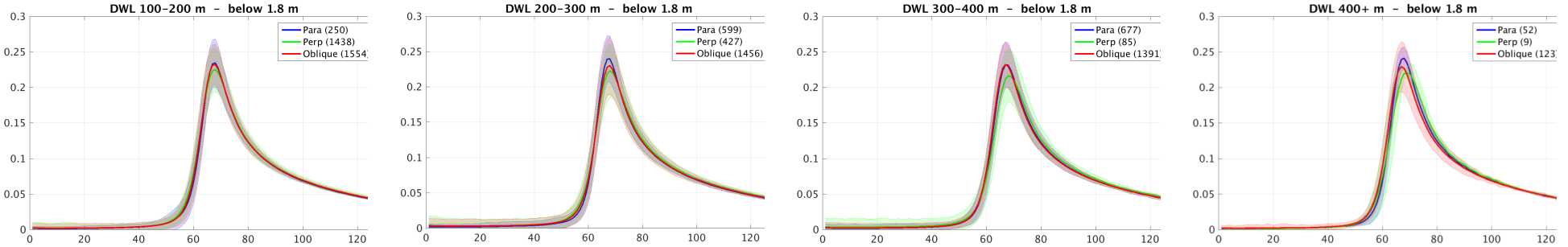

RADS Significant height below 1.8 m

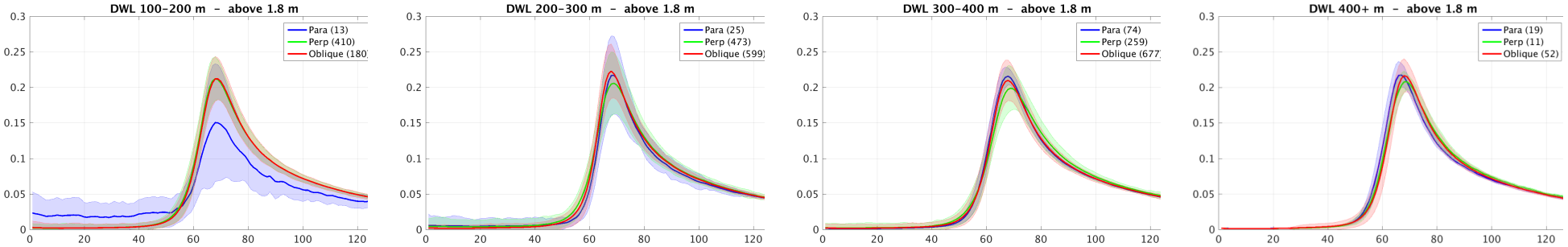

RADS Significant height above 1.8 m

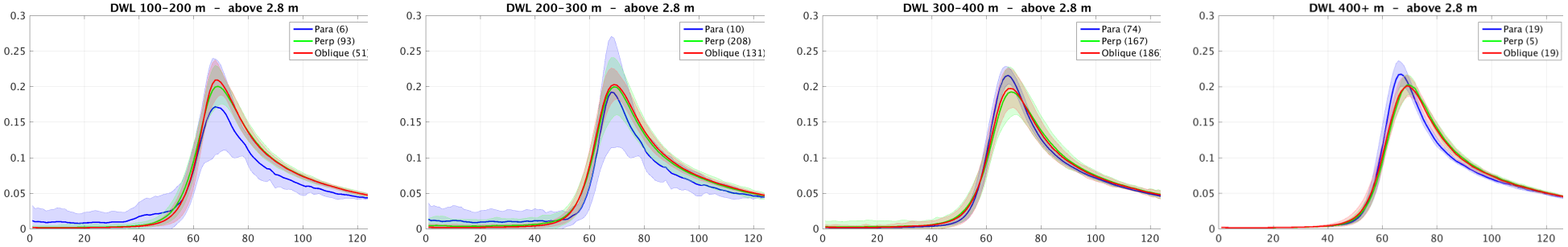

RADS Significant height above 2.8 m

(Caption on next page)

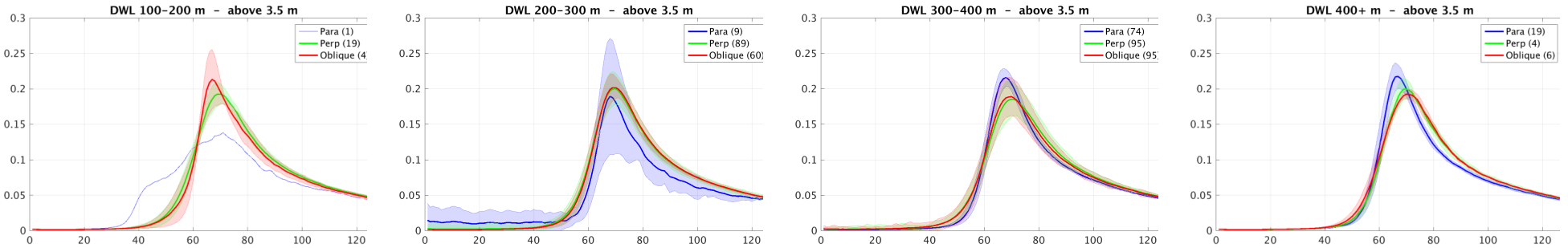

RADS Significant height above 3.5 m

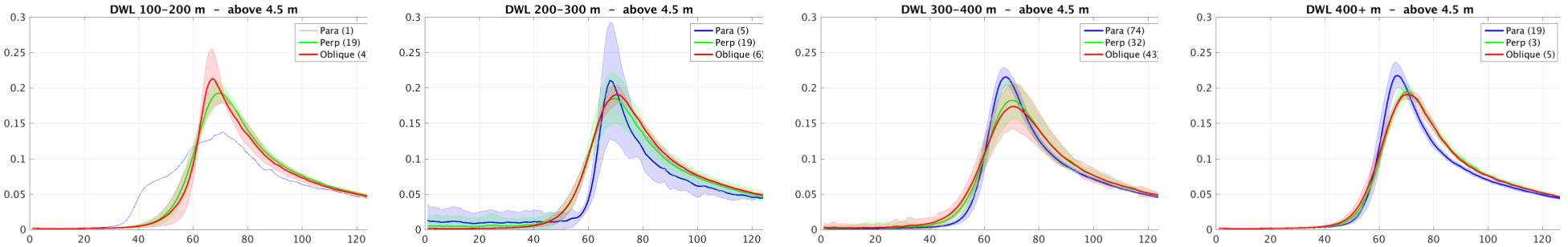

RADS Significant height above 4.5 m

Figure 29 (including previous page): Average Cryosat-2 SAR waveforms in different categories of (rows) dominant swell height and (columns) dominant swell length for (blue) parallel, (green) perpendicular and (red) oblique swell orientation. The number of samples in each category is shown in the legend. The data shown are L1B waveforms obtained with the SARvatore processor optimised for SAR mode ocean altimetry.

4.5. CRYOSAT-2 LEVEL 2 SSH IN DIFFERENT SWELL CONDITIONS

4.5.1. OVERVIEW

Moving on now beyond the analysis of waveform shape, we seek to detect the presence of swell effects on Level 2 SAR altimeter sea surface height (SSH) measurements through possible impact on the retrieved range in SAR mode. Two questions are considered:

- Is there evidence of biases in SAR SSH data that are linked to the presence of swell ?
- Is there evidence that the precision of SAR SSH is affected by swell ?

The first question is addressed by comparing the Cryosat-2 SAR range to the coincident range measured in Pseudo-LRM (PLRM). For this, the Cryosat-2 SARvatore SAR products are collocated with Cryosat-2 Pseudo-LRM data from the Radar Altimeter Database System (RADS; http://rads.tudelft.nl/rads) which provides PLRM measurements for Cryosat-2 in the SAR mode zones. The range difference between SAR mode and PLRM is then examined for different swell categories of swell height, swell length and swell orientation as done previously for the waveform shape analyses. In doing so, the PLRM data effectively serves as a baseline assumed to be insensitive to swell, against which any biases in SAR SSH data can be examined.

The second question is addressed simply by considering the variability (i.e. precision) of the 20Hz SSH and by examining possible dependences on swell conditions. The precision of 20Hz SSH is provided in SARvatore products as a 1Hz field.

4.5.2. CRYOSAT-2 SAR L2 SSH BIASES AGAINST PLRM IN DIFFERENT SWELL CONDITIONS

The comparison of the SAR and PLRM ranging is performed on 1Hz SSH uncorrected for geophysical effects. Since SAR and PLRM are assumed to be exactly collocated, 1Hz geophysical corrections would be the same for the two modes, except for SSB. In this analysis, no correction for SSB was applied to either SAR or PLRM.

Uncorrected 1Hz SSH data are provided in the SARvatore products. These are already corrected for instrument and reference frame offsets and provide estimates of the uncorrected SSH with respect to WGS84.

For RADS, the uncorrected 1Hz SSH has to be computed and brought to the same frame of reference as the SARvatore data. RADS uncorrected SSH is computed as follows:

$$SSH\_unc\_1Hz = alt - (range + ref\_frame\_offset + dh\_ellipsoid) \qquad Eq.\ 6$$

Where alt is the satellite altitude (RADS default field alt_gdrd for Cryosat-2), range is the distance from the centre of the earth to the satellite (RADS default field range_ku for Cryosat-2), ref_frame_offset is a ranging correction to align the data with the Topex reference mission and dh_ellipsoid accounts for the difference between the Topex reference frame and WGS84.

The SAR minus PLRM SSH differences are shown in Figure 30 and Figure 31 against RADS significant wave height and Envisat ASAR dominant swell wave length respectively.

The different subplots correspond to different dominant swell wave height categories. The colours relate to the usual parallel, perpendicular and oblique swell orientation classification. The number of samples in each category is indicated in the legend of each subplot. The mean SSH difference for each swell category is also indicated in each subplot.

On the basis of these results, there is no evidence of biases in SAR ranging due to swell.

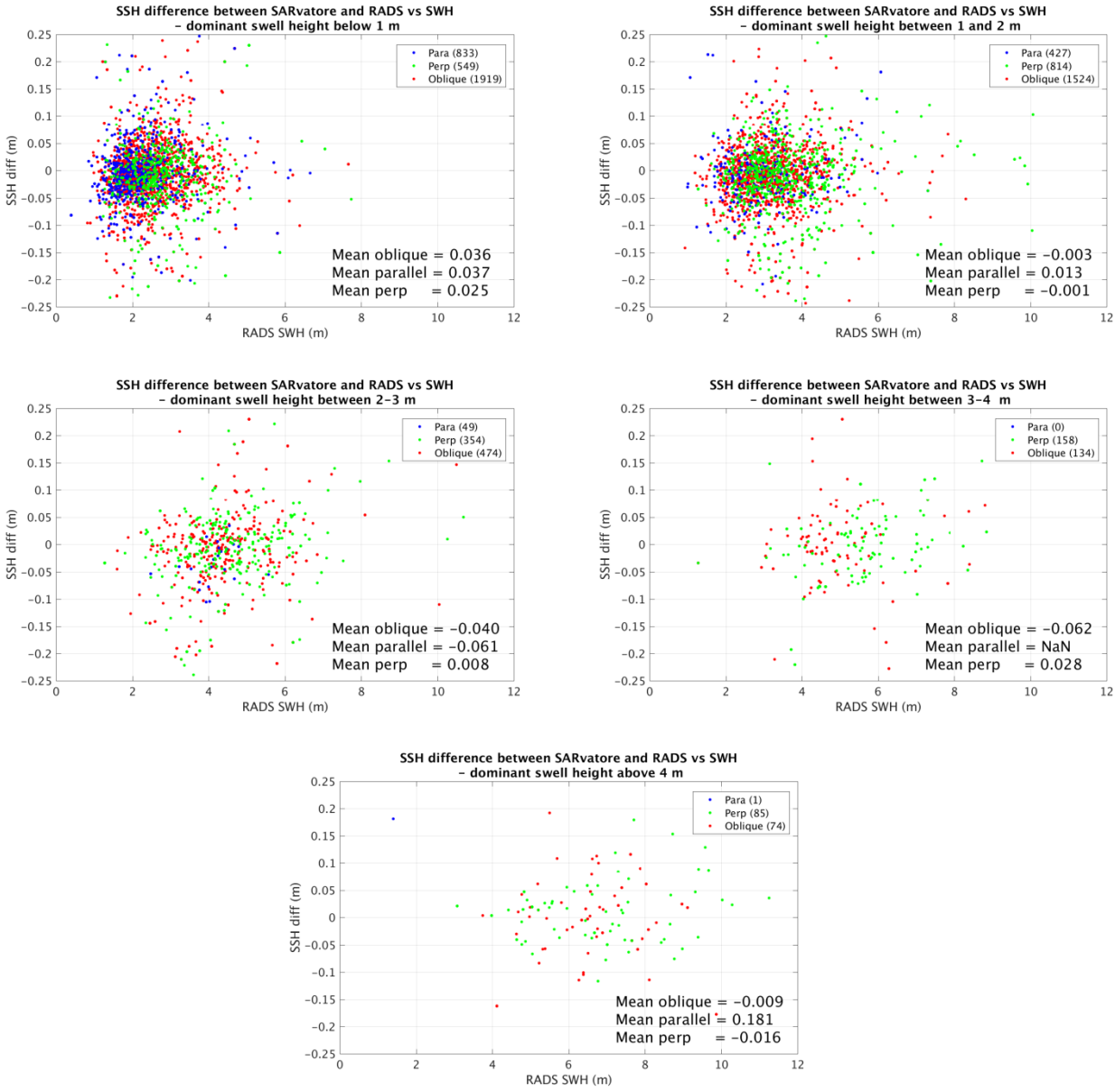

Figure 30: Cryosat-2 1Hz uncorrected SSH differences between SAR mode and collocated RADS PLRM against RADS significant wave height, plotted for different dominant swell height categories, for (blue) parallel, (green) perpendicular and (red) oblique swell orientation.

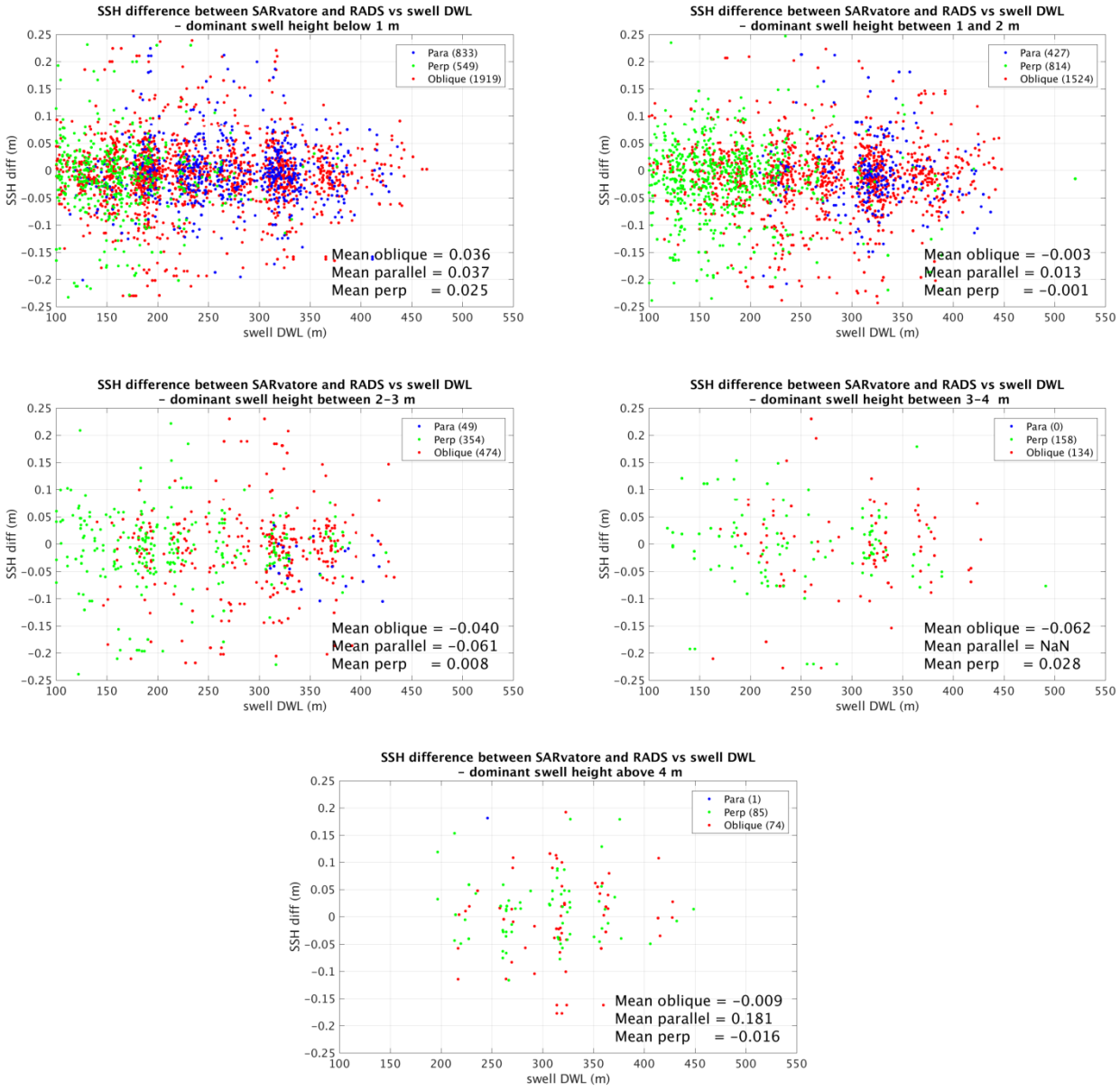

Figure 31: Cryosat-2 1Hz uncorrected SSH differences between SAR mode and collocated RADS PLRM against RADS significant wave height, plotted for different dominant swell height categories, for (blue) parallel, (green) perpendicular and (red) oblique swell orientation.

4.5.3. CRYOSAT-2 SAR SSH PRECISION IN DIFFERENT SWELL CONDITIONS

The SSH precision is provided in the Cryosat-2 SARvatore products as a 1Hz field, and represents the standard deviation of the 20Hz SSH measurements within approximately 1 second. SSH precision is known to be smaller in SAR mode than in LRM and PLRM, and degrades (increases) with increasing significant wave height in all modes. The dependence on swell is however not known.

Figure 32 present the Cryosat-2 SAR SSH precision plotted against RADS SWH for different categories of dominant swell height and swell orientation using the parallel/perpendicular/oblique color code introduced previously. The number of samples in each category is indicated in the legend on each subplot.

In all subplots, a black line with a slope of 1.6mm per metre has been added as a visual reference to help compare the behaviour in each swell category. We note that:

- The black line fits the data well in the lower swell height category but not in higher swell heights. This reflects the fact that increasing swell height is accompanied by increasing significant wave height (and therefore larger precision), and that the increase in precision is not linear with SWH for higher SWH.
- For a given value of SWH, the SSH precision gives similar values regardless of dominant swell height.
- There is no sensitivity to swell orientation, as parallel, perpendicular and oblique show similar behaviour. Note again the very small number of parallel swell cases for swell heights greater than 2-3 metres.

Figure 33 presents the same data now plotted against dominant swell length. There is again a general degradation of the precision as the swell height increases (and therefore SWH increases), but there is no dependence on dominant swell length, nor on swell orientation.

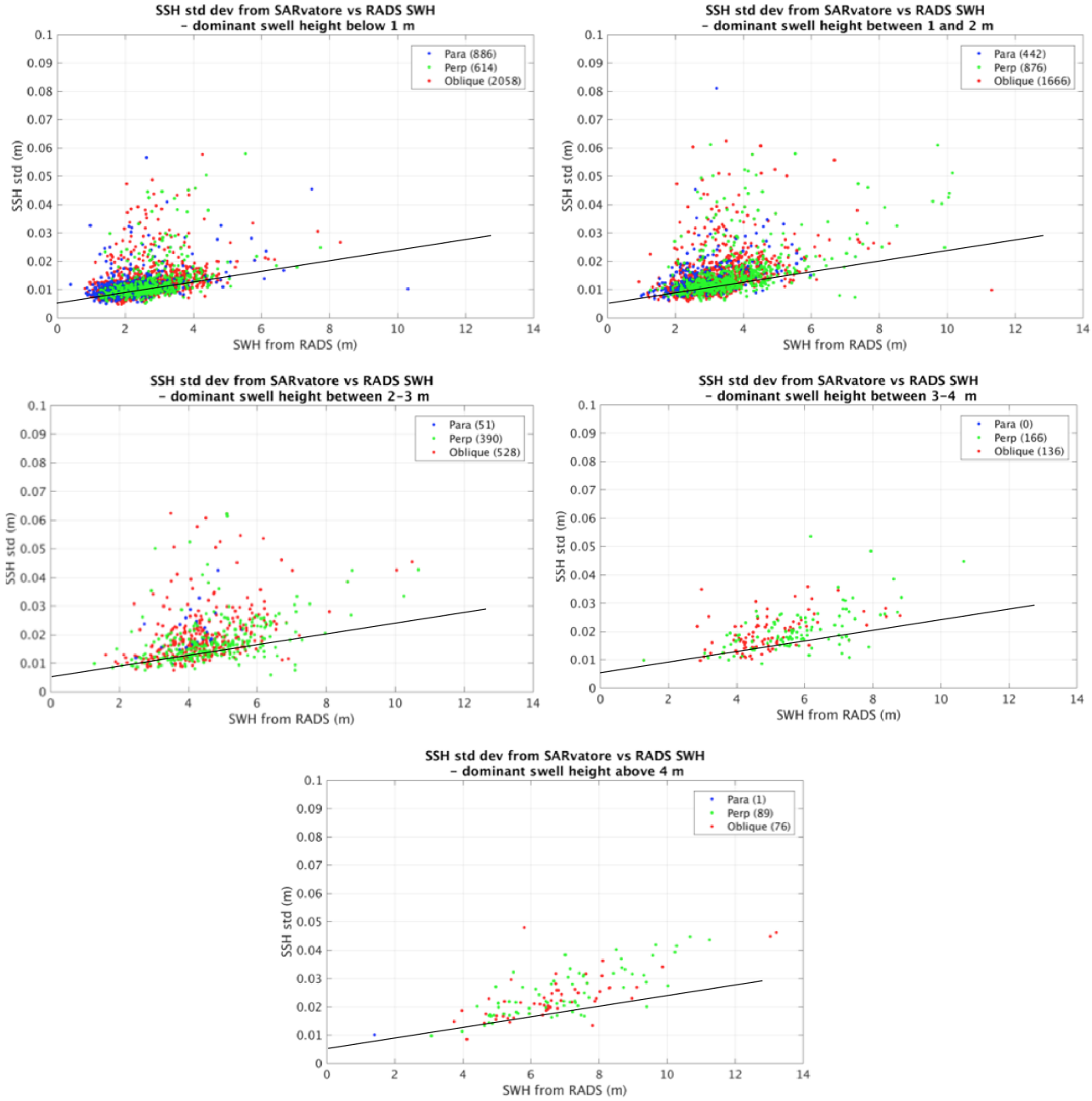

Figure 32: Cryosat-2 SAR SSH variability (20Hz std) against RADS significant wave height, plotted for different dominant swell height categories, for (blue) parallel, (green) perpendicular and (red) oblique swell orientation. The black line has a slope of 1.6mm per metre in all subplots.

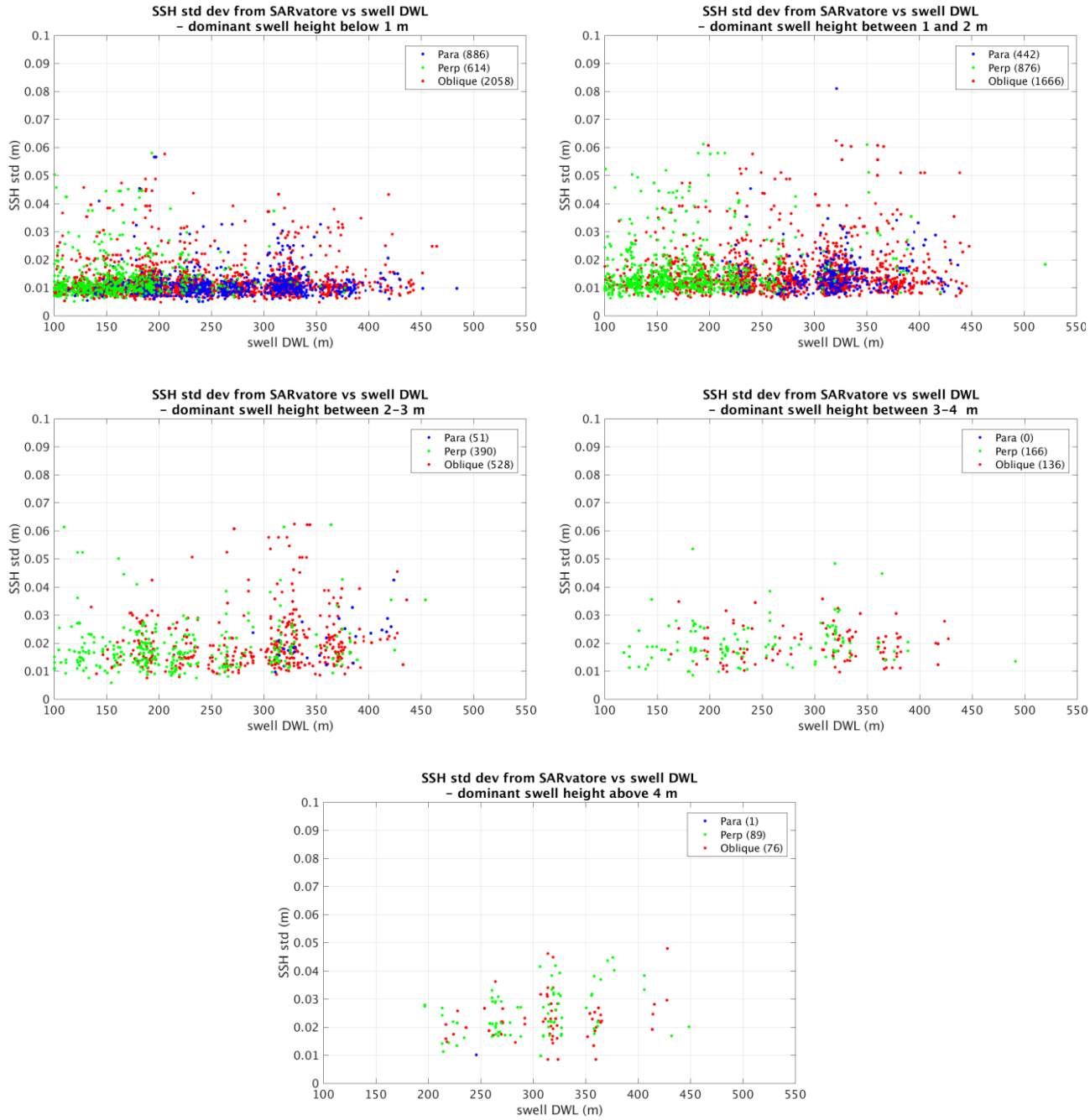

Figure 33: Cryosat-2 SAR SSH variability (20Hz std) against Envisat ASAR dominant wave length, plotted for different dominant swell height categories, for (blue) parallel, (green) perpendicular and (red) oblique swell orientation.

5. ALGORITHMIC BASIS FOR SAR MODE SSB CORRECTION

The scientific investigations presented in previous sections indicate that SAR mode altimetry could be subject to waveform distortion due to swell when swell height is large. The simple modelling used in this study confirms that multi-peaked waveforms could occur in the presence of swell, but that effects become clearly detectable only when swell height exceeds 4 meters, which is relatively rare. In the case of the Cryosat-2 data examined in this study, only 2% of samples satisfied this condition.

Experimental investigations of Cryosat-2 SAR mode data in different swell conditions produced no consolidated evidence of swell effects. Although some anomalous 20Hz waveforms are occasionally observed, these effects are not detected in the overall results for average L1B waveform shapes and L2 1Hz SSH biases and precisions. However, it must be stressed that analyses in this study were limited geographically by the availability of Cryosat-2 SAR mode acquisitions over the ocean and the ability to collocate with Envisat ASAR to obtain swell information. Since absence of evidence is not evidence of absence, it is strongly advised that analyses should be repeated with a broader geographical scope, including in particular data from the central Pacific and the Southern Ocean where high sea state and swell conditions are more prevalent. This could perhaps be achieved by using a similar collocation approach between Sentinel-3 SRTM and Sentinel-1 L2 swell products, should such data be available.

Regarding the estimation of the SAR mode SSB correction, empirical estimation methods offer the only viable way forward at present. Parametric, non-parametric and hybrid methods are all relevant to the development of SAR mode SSB corrections, noting that hybrid methods may provide more robust estimates in those high sea state and swell conditions that are less densely populated and where effects will be more significant.

The development of SAR mode SSB corrections should consider the inclusion of sea state information linked to sea state development, rather than be limited to dependences on wind speed and Hs alone. This would be consistent with the observed tendency for LRM SSB correction to move towards three-parameters SSB models that either use additional external information from a wave model (e.g. Tran et al., 2006; Tran et al., 2010b) or rely on a more thorough exploitation of the sea state information contained in altimeter backscatter coefficient and Hs measurements (e.g. Pires et al., 2016; see Figure 34).

One would want to ascertain the impact of waveform distortion by swell on the estimation of range separately from the impact on SAR mode Hs, which is likely to be more strongly affected. It is worth recalling also that SAR mode Hs is very sensitive to a large number of other factors, not least various processing choices and how platform mispointing is handled.

Finally, regardless of the approach, care should be taken to properly characterise sea state conditions where differences between SAR mode altimetry and conventional altimetry are observed. This will help to avoid indiscriminate attribution of all observed differences in SAR mode altimetry to swell, solely on the basis of geographical location. One important aspect

will be to determine if these impacts are really caused by "swell", in the proper oceanographic meaning of the word, or if they simply reflect the faster, non-linear, degradation of the performance of SAR mode altimetry in high sea states.

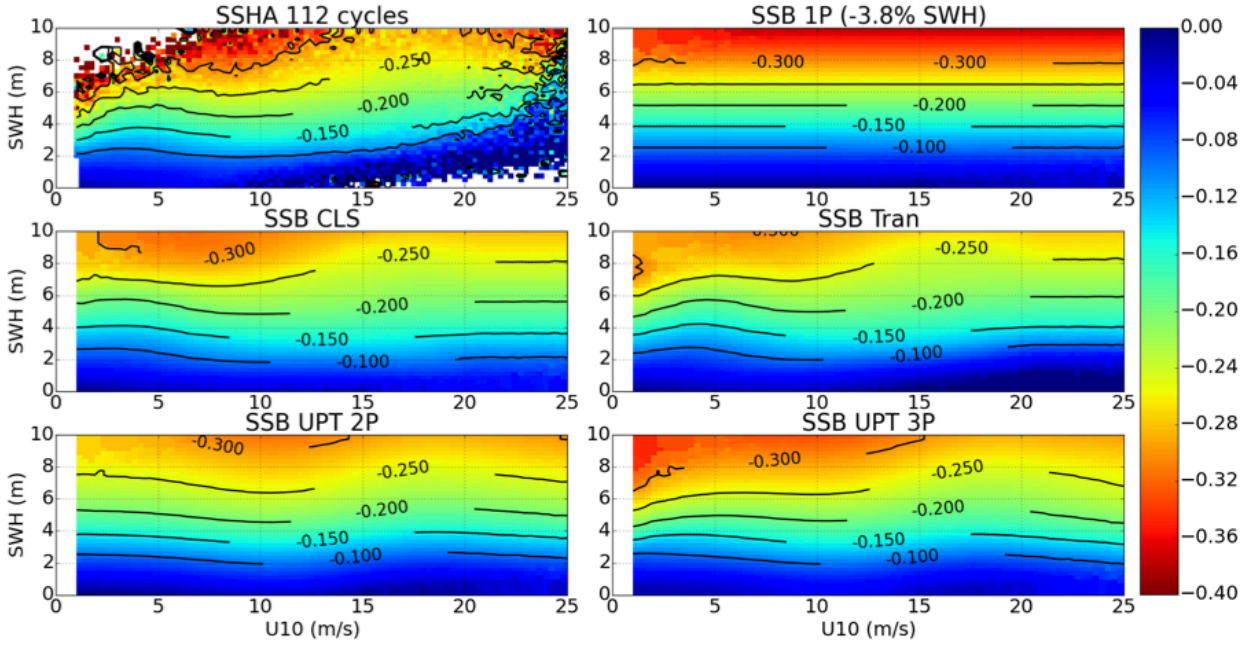

Figure 34: Jason-1 SSB corrections taken from Figure 5 in Pires et al. (2016) showing: (top left) Sea Surface Height Anomaly binned in the Significant Wave height (SWH) and U10 domain; (top right) an empirical model computed as −3.8% of SWH; (middle left) the established SSB model by Gaspar et al. (2002); (middle right) theSSB model by Tran et al. (2010b); (bottom left and right) two- and three-parameter SSB models proposed by Pires et al. (2016).

6. METHODS FOR CALIBRATION AND VALIDATION OF SAR MODE SSB

Validating altimeter SSB correction models has long been a challenge for conventional altimetry, partly because of our incomplete understanding of the processes at play, but mainly because of the difficulties of grappling with this elusive and complex phenomenon. As seen in Section 2.2, theoretical and experimental methods provide some insight into the physical processes involved but have not led to practical ways of estimating ranging errors induced by SSB. Empirical estimation of SSB from the satellite altimeter data themselves is the main approach used today. However, comparing SSB models from different satellite altimeters offers no prospect of validation. Such exercises simply highlight differences linked to instrument behaviour and processing (the so-called tracked bias) that cloud and obscure the underlying similarities in the dependence of SSB on sea state.

In the case of SAR mode altimetry, the challenges to validate SAR mode SSB are the same - i.e. no better, no worse - than for conventional altimetry. Empirical estimation of the SSB

ranging errors directly from the satellite data also appear to offer the best way forward at this stage.

For SAR mode altimetry however, there is an added validation element offered by the ability to process altimeter echoes from SAR altimeter missions also in an incoherent manner similar to LRM. The process, known as SAR reduction or Pseudo-LRM, is illustrated in Figure 35 together with the LRM and SAR processing chains in the case of a Cryosat-2 or Sentinel-3 type altimeter operating in closed-burst SAR mode. Comparison between SAR mode and P-LRM was the basis of the results shown in Section 4.5.2.

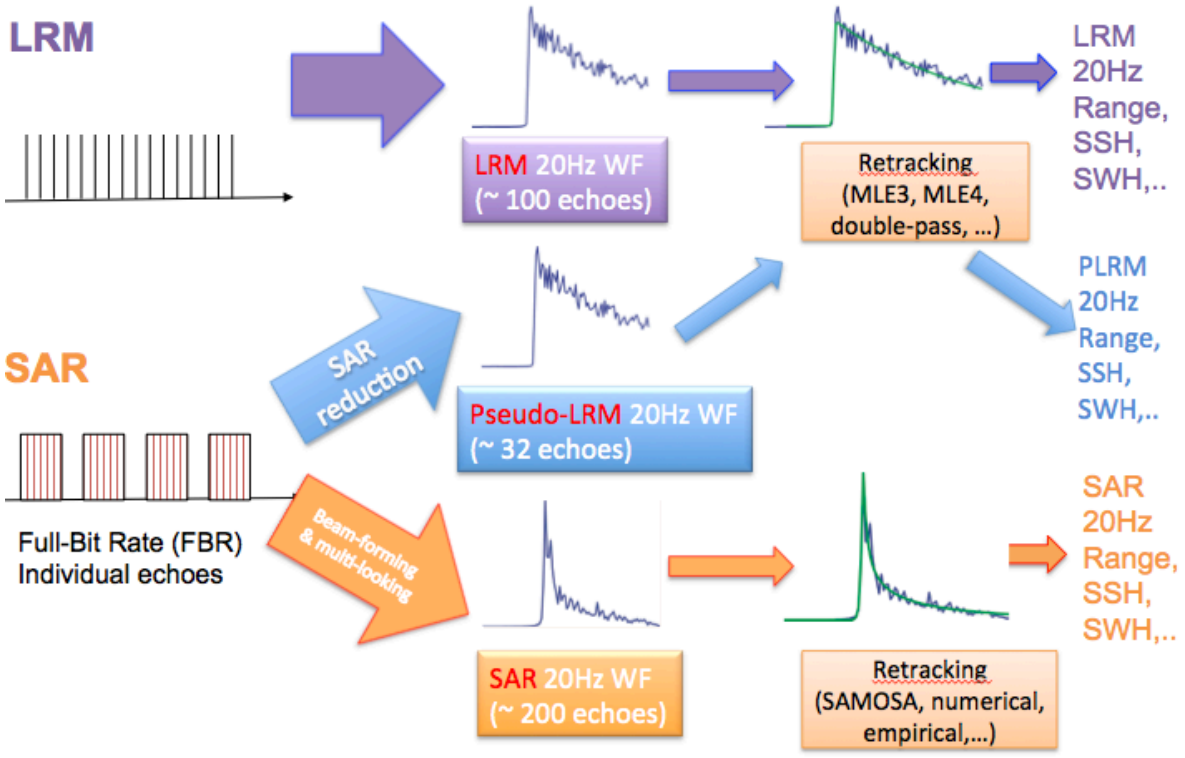

Figure 35: Illustration of the processing chains in LRM, Pseudo-LRM (P-LRM) and SAR mode altimetry. The example shows the case of closed-burst SAR mode altimetry as used on Cryosat-2 and Sentinel-3. In the case of interleaved SAR mode, as used on Sentinel-6/Jason-CS, the individual echoes are transmitted continuously and the "reconstructed" P-LRM are exactly equivalent to LRM.

Notwithstanding the increased noise (precision) in the P-LRM data for SAR mode altimeters operating in closed-burst mode, it has been shown with Cryosat-2 that P-LRM range measurements are unbiased against conventional LRM. This opens the possibility of comparing SAR mode data directly with coincident LRM-type data, offering a unique way of calibrating and validating SAR mode SSB against conventional altimetry while, conversely, giving the means of understanding differences between SAR mode and LRM altimetry.

In the case of Sentinel-6/Jason-CS, the instrument will operate in the so-called SAR Interleaved mode characterised primarily by a continuous PRF rather than a burst-type chronogram (see Figure 36). Hence, for interleaved SAR mode instruments, true LRM data that are exactly equivalent to LRM from contemporary and past conventional altimeter missions can be obtained without the loss of precision seen for burst-mode P-LRM. The Jason-CS SAR mode data will therefore be comparable directly with coincident true LRM that make it possible to tie the Jason-CS SAR mode mission to the long-term altimetric data record. This was one of the main motivation of the recommendations put forward by Gommenginger et al., (2013a) in support of SAR Interleaved mode for Sentinel-6/Jason-CS.

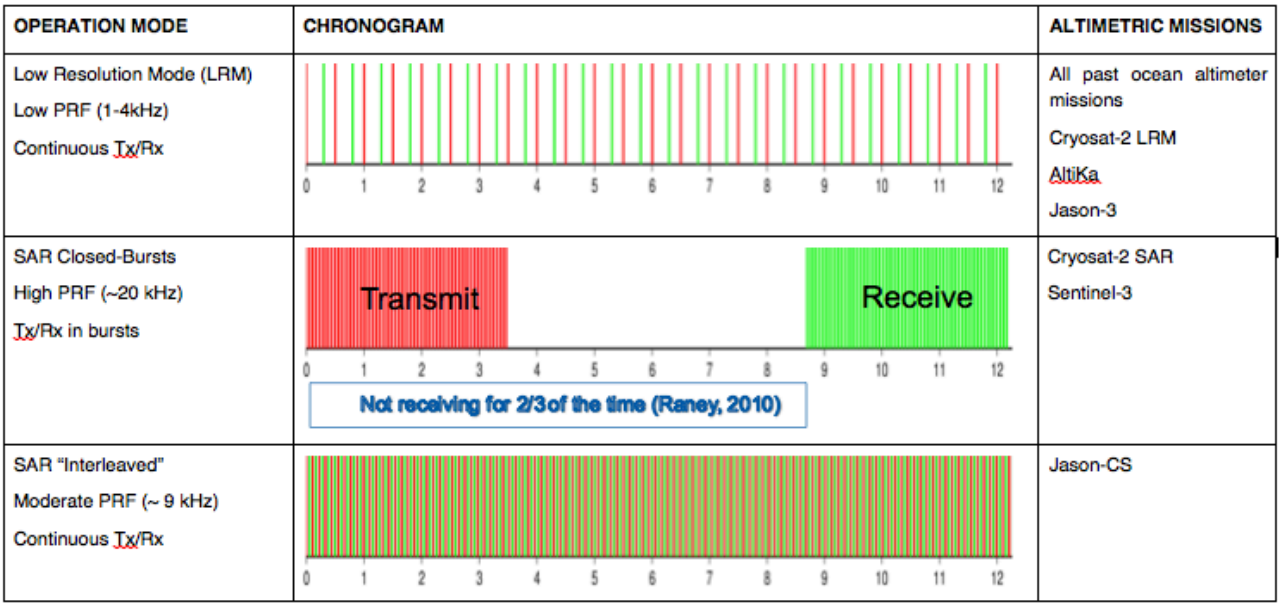

Figure 36: Chronograms for (top) LRM (middle) Closed-Burst SAR and (bottom) Interleaved SAR altimeters (from Gommenginger et al, 2013a).

7. LIST OF ACRONYMS

aka	also known as
CLS	Collecte Localisation Satellites
CPP	Cryosat-2 Prototype Product (produced by CNES)
LUT	Look-up table
LRM	Low resolution mode (aka pulse-limited, or conventional)
mss	mean square slope (i.e. variance of the sea surface slope)
MSS	Mean Sea Surface
P-LRM	Pseudo-LRM (aka Reduced SAR)
PRF	Pulse repetition frequency
SAR	Synthetic Aperture Radar
SLA	Sea Level Anomaly
SSB	Sea state bias
SSH	Sea surface height
SWH	Significant Wave Height (aka as Hs or $H_{1/3}$)

8. REFERENCES

Amarouche, L., Thouvenot, E. & Chapron, B. 2000 Simulation of altimeter waveforms from a deterministic three dimensional ocean surface, Proc. Geoscience and Remote Sensing Symposium (IGARSS 2000), Honolulu, 24-28 July 2000.

Arnold, D.V., W.K. Melville, R.H. Stewart, J.A. Kong, W.C. Keller, and E. Lamarre 1995 Measurements of electromagnetic bias at Ku and C bands, *J. Geophys. Res.*, *100* (C1), 969-980.

Barrick, D. E. & Lipa, B. J. 1985 Analysis and interpretation of altimeter sea echo, *Adv. Geophys.,* **27,** 61-100.

Boy, F. & Moreau, T. 2013 Algorithm Theoretical Basis Document (ATBD) of the CPP SAR numerical retracker for oceans. CNES report reference S3A-NT- SRAL-00099-CNES, Version 1.0, 15/06/2013, 16 pp.

Cazenave A. & Llovel W. 2010 Contemporary sea rise, Ann. Rev. Mar. Sci., 2, 145-173.

Chelton, D. B. 1994 The sea state bias in altimeter estimates of sea level from collinear analysis of TOPEX data. J. Geophys. Res. 99, 24995–25008.

Chelton D.B., Reis J.C., Haines B.J., Fu L-L. & Callahan P.S. 2001 Satellite Altimetry, Chapter 1 in Fu & Cazenave (2001).

Choy, L.W., D.L. Hammond, and E.A. Uliana 1984 Electromagnetic bias of 10-GHz radar altimeter measurements of MSL, *Marine Geodesy*, **8** , 297-312.

Creamer D.B., Henyey F. Schult R. & Right J. 1989 Improved linear representation of ocean surface waves, J Fluid Mech, 205, 135-161.

Dinardo, S. and J. Benveniste 2013 Guidelines for the SAR (Delay-Doppler) L1b Processing, ESA XCRY-GSEG-EOPS-TN-14-0042, Is. 2.3, 29/05/2013. https://wiki.services.eoportal.org/tiki- download_wiki_attachment.php?attId=2540

EUMETSAT 2014: Statement of Work: Jason-CS SAR Mode Sea State Bias study. Issue v2. Date 27 October 2014. EUMETSAT Reference EUM/TSS/SOW/14/763543. 6 pages.

Elfouhaily, T., D. R. Thompson, B. Chapron, and D. Vandemark 2000 Improved electromagnetic bias theory, J. Geophys. Res., 105, 1299– 1310.

Elfouhaily, T., D. R. Thompson, B. Chapron, and D. Vandemark 2001 Improved electromagnetic bias theory: Inclusion of hydrodynamic modulations, J. Geophys. Res., 106, 4655–4664.

Fu L-L. & Cazenave A. (eds) 2001 Satellite altimetry and Earth sciences: a handbook of techniques and applications, Academic Press, Sn Diego.

Gaspar, P., F. Ogor, P.-Y. Le Traon, and O.-Z. Zanife 1994 Estimating the sea state bias of the TOPEX and POSEIDON altimeters from crossover differences, J. Geophys. Res., 99, 24,981–24, 994.

Gaspar P. & Florens J-P. 1998 Estimation of the sea state bias in radar altimeter measurements of sea level: Results from a new nonparametric method. J. Geophys. Res. 103:15803–15814.

Gaspar P., Labroue S., Ogor F., Lafitte G., Marchal L. & Rafanel M. 2002 Improving nonparametric estimates of the sea state bias in radar altimeter measurements of sea level. Journal of atmospheric and oceanic technology, 19(10), 1690-1707.

Glazman R.E., Fabrikant A. & Srokosz M.A. 1996 Numerical analysis of sea state bias for radar altimetry, J. Geophys. Res.,101, 3789-3799.

Globwave product user guide 2013, Available from: http://globwave.ifremer.fr/download/GlobWave_D.7_PUG3_v1.0.pdf

Gommenginger, C. P., S. Dinardo, P. Cipollini, H. Snaith, D. Cotton and J. Benveniste 2014 SAR altimetry over the ocean and the coastal zone: the new frontier. OSTST 2014, Konstanz, 27-31 October 2014.

Gommenginger, C., Martin-Puig, C., Amarouche, L. & Raney, R. K. 2013a Jason-CS SAR Mode Error Budget Study: Review of State of Knowledge of SAR Altimetry over Ocean. EUMETSAT report EUM/RSP/REP/14/749304, version 2.2, 21 Nov 2013. *http://eprints.soton.ac.uk/366765/1/SARAltimetry_Review_JasonCS_EUMETSAT.*pdf

Gommenginger, C. P., P. Cipollini , H. M. Snaith, L. West, & M. Passaro 2013b SAR altimetry over the open and coastal ocean: status and open issues. Ocean SAR altimetry expert group meeting, National Oceanography Centre-Southampton, UK, 26-27 June 2013.

Gommenginger, C. 2011a WP3200 The SAMOSA2 SAR Retracker & application to CRYMPS and Cryosat2 data. SAMOSA Final Presentation, ESRIN, Frascati, 18 May 2011. http://www.satoc.eu/projects/samosa/docs/SAMOSA-CCN-D13-Final_V13.pdf

Gommenginger, C., C. Martin-Puig , S. Dinardo, D. Cotton, M. Srokosz and J. Benveniste 2011b Improved altimetric accuracy of SAR altimeters over ocean: Observational evidence from Cryosat-2 SAR and Jason-2. OSTST'2011. San Diego.

Gommenginger, C. P. & Srokosz, M.A. 2006 Sea State Bias - 20 Years On. In, 15 Years of progress in radar altimetry, Venice, 13-18 March 2006. Available from: https://www.researchgate.net/publication/242386384_SEA_STATE_BIAS_-_20_YEARS_ON

Gommenginger, C. P., M. A. Srokosz, P. G. Challenor, and P. D. Cotton 2003a Measuring ocean wave period with satellite altimeters: A simple empirical model, Geophysical Res. Lett., 30, doi:10.1029/2003GL017743.

Gommenginger, C. P., M. A. Srokosz, J. Wolf, and P. A. E. M. Janssen 2003b An investigation of altimeter sea state bias theories, J. Geophys. Res.,108(C1), 3011, doi:10.1029/2001JC001174.

Gommenginger, C. P., M. A. Srokosz, P. G. Challenor, and P. D. Cotton 2002 Development and validation of altimeter wind speed algorithms using an extended collocated buoy/Topex dataset., IEEE Transactions on Geoscience and Remote Sensing, 40(2), 251-260.

Gourrion J., Vandemark D., Bailey S.A., Chapron B., Gommenginger C., Challenor P.G. & Srokosz M.A. 2002 A two parameter wind speed algorithm for Ku-band altimeters, J. Atmos. Oceanic Tech., 19, 2030-2048.

Hevizi, L.G., E.J. Walsh, R.E. McIntosh, D. Vandemark, D.E. Hines, R.N. Swift, and J.F. Scott 1993 Electromagnetic bias in sea surface range measurements at frequencies of the TOPEX/POSEIDON satellite, *IEEE Transactions on Geoscience and Remote Sensing*, **31**, 376-388.

Hwang P.A. & Plant W.J. 2010 An analysis of the effects of swell and surface roughness spectra on microwave bacscatter from the ocean, J Geophys. Res., 115, doi:10.1029/2009JC005558

Jackson F.C. 1979 The reflection of impulses from nonlinear random sea, J Geophys. Res. 87(C5), 4939-4943.

Kalantzi, G. D., C. Gommenginger and M. Srokosz 2009 Assessing the performance of the dissipation parameterisations in WAVEWATCH III by using collocated altimetry data. Journal of Physical Oceanography, 29: 2800-2819.

Kumar R., Stammer D., Melville W.K. & Janssen P. 2003 Electromagnetic bias estimates based on Topex, buoy, and wave model data, J Geophys Res, 108, doi:10.1029/2002JC001525

Labroue, S., P. Gaspar, J. Dorandeu, O. Z. Zanife, F. Mertz, P. Vincent, and D. Choquet 2004 Non-parametric estimates of the sea state bias for Jason-1 radar altimeter, Marine Geodesy, 27, 453–481, doi:10.1080/ 01490410490902089.

Lipa, B. J. & Barrick, D. E. 1981 Ocean surface height-slope probability density function from SEASAT altimeter echo, *J. Geophys. Res.,* **86,** 10921-10930.

Longuet-Higgins, M.S. 1963 The effect of nonlinearities on statistical distributions in the theory of sea waves, *Journal of Fluid Mechanics*, **17**, 459-480.

Mackay E.B.L., Retzler C.H., Challenor P.G. & Gommenginger C.P. 2008 A parametric model for ocean wave period from K_u band altimeter data, J. Geophys. Res., 113, doi: 10.1029/2007JC004438.

Melville, W. K., F. C. Felizardo, and P. Matusov 2004 Wave slope and wave age effects in measurements of electromagnetic bias, J. Geophys. Res., 109, C07018, doi:10.1029/2002JC001708.

Melville, W. K., R. H. Stewart, W. C. Keller, J. A. Kong, D. V. Arnold, A. T. Jessup, M. R. Loewen, and A. M. Slinn 1991 Measurements of electro- magnetic bias in radar altimetry, J. Geophys. Res., 96, 4915 – 4924.

Millet F.W., Warnick K.F. & Arnold D.V. 2005 Electromagnetic bias at off-nadir incidence angles, Journal of Geophysical Research, 110, doi:10.1029/2004JC002704

Millet, F. W., D. V. Arnold, K. F. Warnick, and J. Smith 2003a Electromagnetic bias estimation using in situ and satellite data: 1. RMS wave slope, J. Geophys. Res., 108(C2), 3040, doi:10.1029/2001JC001095.

Millet, F. W., D. V. Arnold, P. Gaspar, K. F. Warnick, and J. Smith 2003b Electromagnetic bias estimation using in situ and satellite data: 2. A non-parametric approach, J. Geophys. Res., 108(C2), 3041, doi:10.1029/2001JC001144.

Millet R.W., Warnick K.F., Nagel J.R. & Arnold D.V. 2006 Physical Optics-Based Electromagnetic Bias Theory With Surface Height–Slope Cross-Correlation and Hydrodynamic

Modulation, IEEE Trans Geosci Remote Sensing, 44, 1470-1483.

Moreau, T., S. Labroue, P. Thibaut, L. Amarouche, F. Boy, & N. Picot 2013 Sensitivity of SAR Mode Altimeter to Swell Effect. Cryosat Third User Workshop, Dresden, 12-14 March 2013.

Naenna P. & Johnson J.T. 2010 A Monte Carlo study of altimetere pulse return and electomagnetic bias, IEEE Trans Geosci Remote Sensing, 48, 3218-3224.

Nerem S., Leuliette E. & Cazenave A. 2006 Present-day sea-level change: A review, Comptes Rendus Geoscience, 338, 1077-1083.

Pires N., Fernandes M. J., Gommenginger C. & Scharroo R. 2016, A Conceptually Simple Modeling Approach for Jason-1 Sea State Bias Correction Based on 3 Parameters Exclusively Derived from Altimetric Information. Remote Sensing, 8(7), 576.

Quartly, G. D., M. A. Srokosz, and A. C. McMillan. 2001. 'Analyzing Altimeter Artifacts: Statistical Properties of Ocean Waveforms'. *Journal of Atmospheric and Oceanic Technology* 18 (12): 2074–91. doi:10.1175/1520-0426(2001)018<2074:AAASPO>2.0.CO;2.

Ray, C., C. Martin-Puig, M. P. Clarizia, G. Ruffini, S. Dinardo, C. Gommenginger and J. Benveniste 2014 SAR Altimeter Backscattered Waveform Model, IEEE Trans. GeoSci. & Rem. Sens., Vol. 53, Iss. 2., pp 911 – 919. doi: 10.1109/TGRS.2014.2330423.

Scharroo, R. & J. Lillibridge 2004 Non-parametric sea-state bias models and their relevance to sea level change studies, Proc. 2004 Envisat & Ers Symposium, Salzburg, 6-10 Sept 2004.

Srokosz, M. 1986 On the joint distribution of surface elevation and slopes for a nonlinear random sea, with an application to radar altimetry, J. Geophys. Res., 91, 995–1006.

Stewart, R.H., and B. Devalla 1994 Differential sea-state bias: A case study using TOPEX / POSEIDON data, *Journal of Geophysical Research*, **99**, 25009-25013.

Stopa J.E., Ardhuin F., Babanin A. & Zieger S. 2015 Comparison and validation of physical wave parameterizations in spectral wave models, Ocean Mod., doi:10.1016/j.ocemod.2015.09.003.

Stopa, J. E., F. Ardhuin, B. Chapron, and F. Collard 2015b, Estimating wave orbital velocity through the azimuth cutoff from space-borne satellites, J. Geophys. Res. Oceans, 120, 7616– 7634, doi:10.1002/2015JC011275.

Tran N., Vandemark D., Chapron B., Labroue S., Feng H., Beckley B. & Vincent P. 2006, New models for satellite altimeter sea state bias correction developed using global wave model data. Journal of Geophysical Research: Oceans, 111(C9).

Tran N., Labroue S., Philipps S., Bronner E. & Picot N. 2010a Overview and update of the sea state bias corrections from the Jason-2, Jason-1 and TOPEX missions, Marine Geodesy, 33, 348-362.

Tran, N., D. Vandemark, S. Labroue, H. Feng, B. Chapron, H. L. Tolman, J. Lambin, and N. Picot 2010b Sea state bias in altimeter sea level estimates determined by combining wave model and satellite data, J. Geophys. Res., 115, C03020, doi:10.1029/2009JC005534.

Vandemark D., Chapron B., Elfouhaily T. and Campbell J.W. 2005 Impact of high-frequency waves on the ocean altimeter range bias, J. Geophys. Res., 110, doi:10.1029/2005JC002979.

Vandemark, D., N. Tran, B. D. Beckley, B. Chapron, and P. Gaspar 2002 Direct estimation of sea state impacts on radar altimeter sea level measurements, Geophys. Res. Lett., 29(24), 2148, doi:10.1029/ 2002GL015776.

Verron J. et al. 2015 The SARAL/AltiKa altimetry satellite mission, Mar. Geod., 38, suppl., 2-21.

Walsh, E.J., D.W. Hancock, D.E. Hines, and J.E. Kenney 1984 Electromagnetic bias of 36-GHz radar altimeter measurements of MSL, *Marine Geodesy*, **8**, 265-296.

Walsh, E.J., F.C. Jackson, D.E. Hines, C. Piazza, L.G. Hevizi, D.J. McLaughlin, R.E. McIntosh, R.N. Swift, J.F. Scott, J.K. Yungel, and E.B. Frederick 1991 Frequency dependence of electromagnetic bias in radar altimeter sea surface range measurements, *Journal of Geophysical Research*, **96**, 20571-20583.

Yaplee, B.S., A. Shapiro, D.L. Hammond, B.D. Au, and E.A. Uliana 1971 Nanosecond radar observations of the ocean surface from a stable platform, *IEEE Trans Geoscience and Electronics*, **9**, 170-174.

Zieger S., J. Vinoth, and I. R. Young, 2009 Joint Calibration of Multiplatform Altimeter Measurements of Wind Speed and Wave Height over the Past 20 Years. *J. Atmos. Oceanic Technol.*, **26**, 2549–2564.